Journal of Materials Chemistry A

ROYAL SOCIETY OF CHEMISTRY

REVIEW

View Article Online
View Journal | View Issue

Cite this: J. Mater. Chem. A, 2023, 11, 13107

Recent advances in MXenes: beyond Ti-only systems

Sandhya Venkateshalu, [a] Mohammed Shariq,[b] Byeongyoon Kim, [a] Monika Patel,[c] Kajal Shakil Mahabari,[c] Sang-Il Choi, *[d] Nitin K. Chaudhari, *[c] Andrews Nirmala Grace*[b] and Kwangyeol Lee *[a]

Received 16th March 2023
Accepted 19th May 2023

DOI: 10.1039/d3ta01590d

rsc.li/materials-a

Since the first report on $Ti_3C_2T_x$ in 2011, the number of reports on 2D transition metal carbides and nitrides, known as MXenes, has increased rapidly. Most of the reports have focused on Ti-based MXenes due to their ease of synthesis and striking properties; however, MXenes beyond Ti-only systems have also been recently reported to exhibit intriguing electronic, magnetic, optical, and mechanical properties. This forward-looking review aims to summarize the research trends, synthesis, properties, and applications of non-Ti MXenes to motivate researchers to unearth the characteristics and unleash the full potential of less explored MXenes. Furthermore, the properties and applications of theoretically predicted non-Ti MXenes are also highlighted to stimulate further research in synthesizing them experimentally. Finally, the challenges to be addressed and future research directions are presented.

1. Introduction

The discovery of the 2D material graphene in 2004 led to extensive research on various other 2D materials such as transition metal dichalcogenides, hexagonal boron nitride (h-BN), metal oxides, phosphorene, germanene, silicene, and so on, enabling technological breakthroughs in a myriad of applications.[1–9] A new class of 2D materials consisting of transition metal carbides and/or nitrides called MXenes have established themselves as some of the most promising materials owing to their exquisite properties.[10] $Ti_3C_2T_x$ was the first

[a]Department of Chemistry, Research Institute for Natural Sciences, Korea University, Seoul 02841, Republic of Korea. E-mail: kylee1@korea.ac.kr
[b]Centre for Nanotechnology Research, Vellore Institute of Technology (VIT), Vellore 632014, Tamil Nadu, India. E-mail: anirmalagrace@vit.ac.in
[c]Department of Chemistry, School of Technology, Pandit Deendayal Energy University, Gandhinagar 382007, Gujarat, India. E-mail: nitin.chaudhari@sot.pdpu.ac.in
[d]Department of Chemistry, Green-Nano Materials Research Center, Kyungpook National University, Daegu 41566, Republic of Korea. E-mail: sichoi@knu.ac.kr

Dr Sandhya Venkateshalu received her Master's degree in Nanotechnology from Visvesvaraya Technological University, India, in 2015. Afterward, she worked as an Assistant Professor for a year at the Dr T. Thimmaiah Institute of Technology, India. She received her Ph.D. in Nanotechnology from the Vellore Institute of Technology, India, in 2021. She is currently a Research Professor at Korea University, Republic of Korea. Her research interests include the synthesis and characterization of nanomaterials, 2D nanomaterials, MXenes, and energy storage and conversion devices.

Dr Mohammed Shariq is an Institute Post-Doctoral Fellow at the Vellore Institute of Technology, India. Prior to joining VIT in 2021, he was a Sandwich Erasmus Doctoral Scholar (2015–2020) from the Department of Mechanical Engineering, Indian Institute of Technology (ISM) Dhanbad, India in collaboration with the IME Institute of Metal Processing and Recycling, RWTH Aachen Germany and University of Maribor, Slovenia. He received his M. Tech in Mechanical Engineering from IIT(ISM) Dhanbad in 2015. His research focuses on the formulation and characterization of novel metal and carbon nanomaterial-based inks, including MXenes, for different 3D printing techniques.

MXene to be discovered and has been under prime focus as a representative member of the MXene family.[11–17] The $Ti_3C_2T_x$ MXene could easily be synthesized by subjecting the Ti_3AlC_2 MAX phase to wet chemical etching with hydrofluoric acid (HF) or etchants that form *in situ* HF. With rich surface chemistry, the representative $Ti_3C_2T_x$ MXene exhibits superior Young's modulus (80–100 GPa),[18] tensile strength (670 MPa),[18] chemical and thermal stability,[19,20] conductivity (20 000 S cm^{-1}),[21] biocompatibility,[22] visible light activity,[23] and electrochemical,[24,25] plasmonic and thermoelectric properties.[26,27]

Although the tremendous interest in Ti-based MXenes is understandable, considering the synthetic ease and their striking properties, the unknown and potentially highly desirable properties of non-Ti MXenes, which include monometallic MXenes besides the Ti-based ones and double transition metal (DTM) MXenes, might also present enormous opportunities for material scientists. The non-Ti MXenes exhibit improved structural stability and different magnetic, electronic, and optical behaviors compared to their Ti counterparts.[28–30] The non-Ti MXenes are also reported to exhibit superior electrochemical properties desirable for energy storage and conversion devices.[31] As the properties of MXenes could be tuned by varying the composition and thickness of MXene layers, new and surprising properties can be expected to be discovered by exploring non-Ti MXenes.

Therefore, this review aims to encourage researchers working on MXenes to unveil the properties of non-Ti MXenes and develop their useful applications. Herein, we comprehensively overview all the synthesized and predicted non-Ti MXenes. The significant breakthroughs in their synthesis, exceptional properties, and applications of non-Ti MXenes are discussed and compared with Ti-based MXenes. Furthermore, the unique properties and applications of theoretically predicted MXenes are also elaborated to stimulate further research in realizing them experimentally. Finally, the current challenges and prospects of non-Ti MXenes are provided.

2. Introduction of MXenes

2D MXenes with a general formula of $M_{n+1}X_nT_x$ are obtained by etching the A element from their 3D parent MAX phase with a general formula of $M_{n+1}AX_n$.[32] The parameters M, A, X, T_x, and n in the general formulae are designated as the transition metal element, group IIIA or IVA element, carbon and/or nitrogen, surface terminations (–O,–OH, and –F), and variable integer

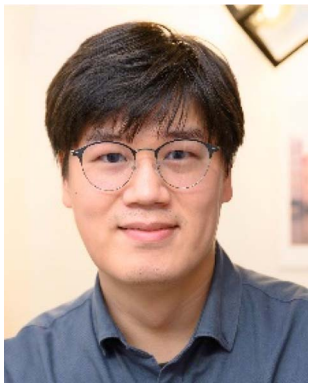

Dr Byeongyoon Kim received his Ph.D. degree (2018) in Chemistry from Korea University, Republic of Korea. Currently, he is working as a postdoctoral fellow with prof. Kwangyeol Lee at the Nano Chemistry Laboratory, Korea University. His research interests include the crystallographic design and synthesis of transition metal-based functional nanomaterials and the applications of electrocatalysis.

Monika Patel is currently pursuing her Ph.D. degree under the supervision of Dr Nitin Chaudhari at the Department of Chemistry, Pandit Deendayal Energy University, Gandhinagar, India. She received her Master's degree from the Department of Chemistry, Gujarat University, Ahmedabad, India in 2018. Her research interests include the development of 2D MXene-based hybrid nanostructured materials as ideal electrode materials for electrochemical energy storage and conversion systems.

Kajal Mahabari received her MSc in Nanoscience and Technology from Chatrapti Shivaji University, Kolhapur, India. She has been working as a Project Associate since 2022 at Pandit Deendyal Energy University, Gandhinagar, India. Her research interests focus on the synthesis of 2D nanomaterials and nanocomposites for energy storage and conversion applications. Also, her interests include the development of an electrocatalyst for electrochemical and photocatalytic water splitting for hydrogen generation and photocatalytic dye degradation.

Prof. Sang-Il Choi received his Ph.D. degree in inorganic chemistry from the KAIST (2011). After his postdoctoral research in the Xia group at the Georgia Institute of Technology, USA, he joined Kyungpook National University in 2015 as a professor. He is the recipient of the 2018 POSCO TJ Park Science Fellowship. His research interests include the design and synthesis of nanocatalysts and the exploration of their applications in electro-catalysis.

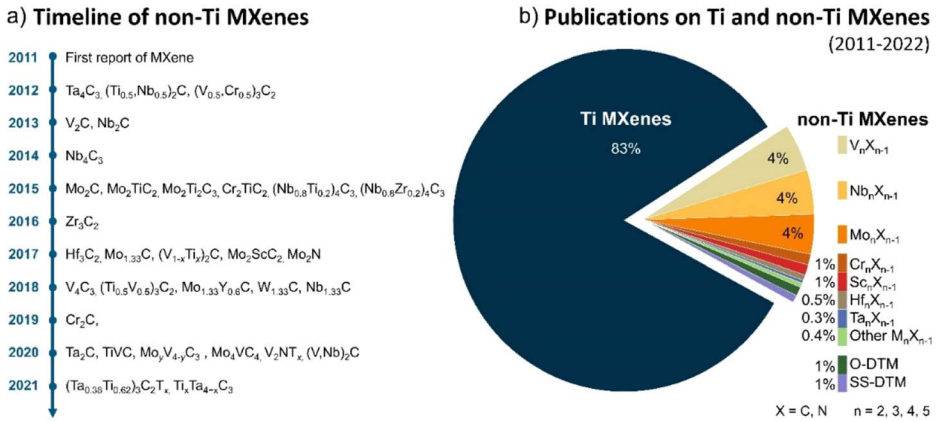

Fig. 1 (a) Timeline of the expansion of the MXene family beyond Ti-only systems. (b) Comparison of the number of publications on Ti and non-Ti MXenes from 2011 to 2022 (source: Web of Science). O-DTM indicates ordered DTM MXenes and SS-DTM indicates solid solution DTM MXenes.

(1–3), respectively.[32,33] By utilizing the difference in the bond strength between M–A and M–X, the A atoms in the MAX phase sandwiched between the MX layers could be selectively etched to produce MXenes, which inherit the hexagonal structure with $P6_3/mmc$ symmetry from their parent MAX phase.[33] By varying the parameters M, A, and X, 155 MAX phase compositions have been synthesized; however, only limited examples of MXenes have been produced from them.[34]

Based on the parameter 'X' in the formula of MXenes, carbide, nitride, or carbonitride MXenes could be obtained. By varying the composition of MXenes, unique properties could be imparted to them. While the carbide MXenes are easily synthesized, the nitride and carbonitride MXenes face difficulties in their synthesis due to the presence of strong bonds.[35] It is important to note that Ti_3CNT_x and $Ti_2C_{0.5}N_{0.5}T_x$ are the only experimentally synthesized carbonitride MXenes as of today.[33,36] Irrespective of the parameter 'X', MXenes could be classified based on the composition of transition metals as monometallic and double transition-metal (DTM) MXenes. In this section, recently developed non-Ti MXenes are briefly introduced.

2.1 Expansion of the MXene family

The timeline of non-Ti MXenes shown in Fig. 1a indicates the tremendous expansion of the MXene family, with new members added almost every year since their discovery. According to the Web of Science, as shown in Fig. 1b, the number of publications on Ti MXenes over the past 10 years is incomparably high compared to non-Ti MXenes. Although there has been relative apathy to non-Ti MXenes among researchers, research interest has been growing recently because the non-Ti MXenes exhibit more intriguing properties than the conventional Ti-based ones.[28–31,37] In the case of monometallic non-Ti MXenes, V_2CT_x, Nb_2CT_x, Mo_2CT_x, Ta_2CT_x, $Zr_3C_2T_x$, $Hf_3C_2T_x$, $Nb_4C_3T_x$, $V_4C_3T_x$, $Ta_4C_3T_x$, V_2NT_x, and Mo_2NT_x have been experimentally synthesized to date and showed interesting physicochemical properties.[28,33,38–43] For example, the $Zr_3C_2T_x$ MXene exhibits

Dr Nitin Chaudhari is an Associate Professor at Pandit Deendayal Energy University, Gandhinagar, India. He received his Ph.D. degree in Materials Science from Korea University, South Korea in 2013. He subsequently worked as a Research Professor at Myongji University and Korea University, South Korea from 2013 to 2019. Later, he joined Nexcoms Ltd. Co., South Korea as a Deputy Director before moving to India. His research interests include the design and development of active electrode materials such as porous carbons, nanocomposites, oxides, sulphides, hydroxides, 2D MXenes, and nanomaterials for energy storage and conversion devices.

Professor Andrews Nirmala Grace is the Director at the Centre for Nanotechnology Research, Vellore Institute of Technology (VIT), Vellore, India. She received her Ph.D. degree from the University of Madras, India, and worked as a Post-doctoral/Senior Researcher Fellow at the Korea Institute of Energy Research, South Korea on Renewable Energy. She is a Fellow of the Royal Society of Chemistry (FRSC) and a Fellow of the Academy of Sciences, Chennai (FASCh). Her current research interests include 2D energy materials, design and fabrication of electrodes for solar cells, and supercapacitors.

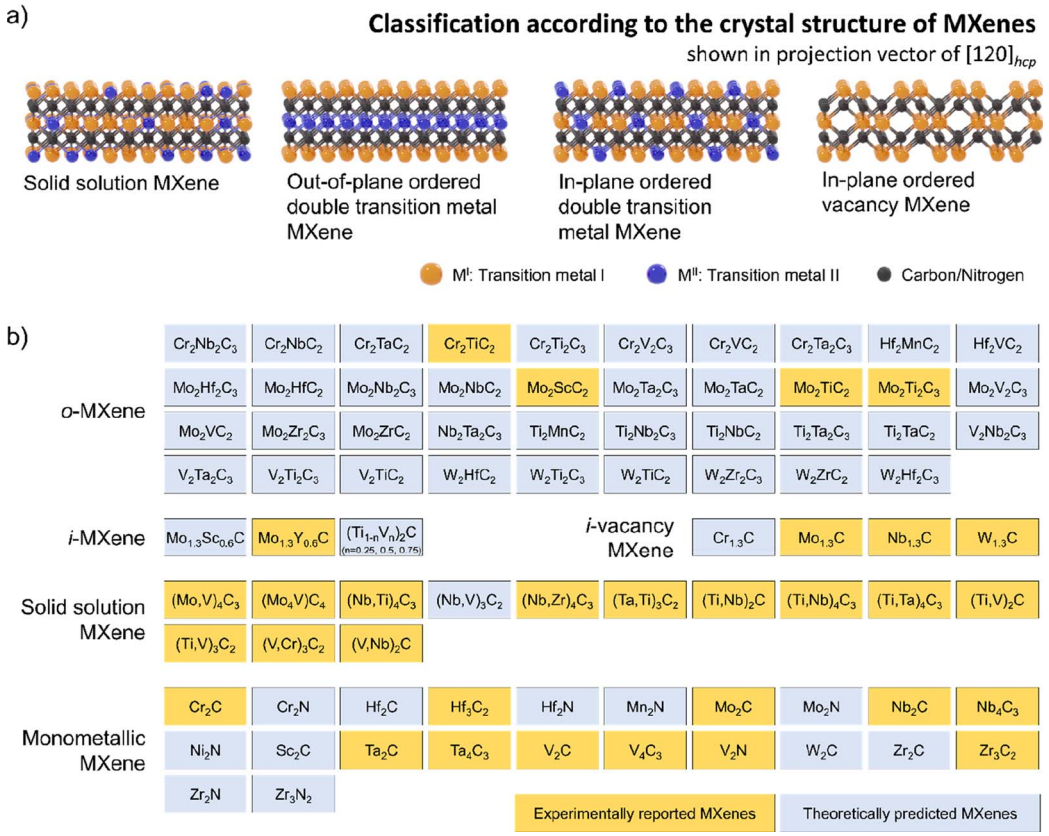

Fig. 2 (a) Schematic illustration of DTM MXenes. (b) The experimentally synthesized and theoretically predicted non-Ti MXenes to date.

better structural stability than $Ti_3C_2T_x$.[28] Cr_2N MXene is predicted to be ferromagnetic in contrast to the antiferromagnetic $Ti_3C_2T_x$,[29,37] and V_2CT_x has higher lithium storage capacity than Ti_2CT_x.[31] Most importantly, with a smaller lateral flake size and the same monolayer thickness as Ti_2C, Nb_2C MXene degrades slower in water, indicating that the chemical properties of MXenes depend on their composition and the type of bond within the monolayer.[44]

Professor Kwangyeol Lee obtained his Ph.D. degree (1997) in Chemistry from the University of Illinois at Urbana–Champaign. After fulfilling his military obligation, he joined Korea University in 2003 as a chemistry faculty member, before being appointed as a professor. He is the recipient of the Wiley-KCS Young Scholar Award (2009, Korean Chemical Society) and the Excellent Research Award (2019, KCS Inorganic Chemistry Division). His current interests include the development of synthetic methodologies for nanoscale materials and the development of nanotechnologies to support the environment by creating sustainable energy.

In 2014, the family of MXenes expanded with the first report on the DTM MAX phase Cr_2TiAlC_2 consisting of two metals at the M site.[45] Based on the arrangement of the two metals M′ and M″ in the structure of MXene, DTM MXenes are further classified as ordered DTM MXenes and random solid solution DTM MXenes (Fig. 2a).[46,47] When the two metals are distributed at specific sites in the M layers, they form ordered DTM MXenes, which are further classified as in-plane (i-MXene) and out-of-plane (o-MXenes) ordered DTM MXenes.[46,48,49] In an i-MXene represented as $(M'_{4/3}M''_{2/3})XT_x$, the two metals are ordered in alternating sites of the same M layer, whereas in the case of o-MXenes represented as $(M'_2M'')X_2T_x$ and $(M'_2M''_2)X_3T_x$, the two metals M″ and M′ are ordered in two separate atomic planes, with M″ and M′ atoms forming the inner and the outer layers, respectively.[48,50,51] Furthermore, when the M″ layer is etched along with the A layers in the i-MAX phase, they form divacancy-ordered MXenes represented as $M'_{4/3}XT_x$.[52,53]

The experimentally synthesized ordered out-of-plane MAX (o-MAX) phases known thus far are Cr_2TiAlC_2,[45,54] Mo_2TiAlC_2,[55] $Mo_2Ti_2AlC_3$,[56] and Mo_2ScAlC_2.[51] The o-MXenes were successfully synthesized by etching the Al layers of these o-MAX phases.[48,51,57] The outer and inner layers of o-MXenes are composed of M′ and M″, respectively, and the C atoms occupy the octahedral sites between the two layers. In contrast to o-MXenes, the i-MXenes reported so far are of lower order M_2XT_x, where M = M′ and

M″.[47] The i-MXenes were obtained by etching the A element of the in-plane ordered MAX (i-MAX) phases.

When the two metals M′ and M″ are randomly distributed at the M site (disordered), they form solid-solution DTM MXene represented as $(M',M'')_{n+1}X_nT_x$.[58,59] Random solid solution DTM MXenes have been reported for all orders of MXenes from M_2C to M_5C_4 (M here represents two metals, M′ and M″).[33,59–63] For simplicity, random solid solution DTM MXenes are referred to as solid solution MXenes hereon. By controlling the stoichiometric ratio of M′ : M″ in the solid solution MXene precisely represented as $(M'_yM''_{1-y})_{n+1}C_nT_x$ $(0 < y < 1)$, different MXene compositions with different properties could be obtained.[47] The random solid solution DTM MAX phases such as $(Cr_{0.5}V_{0.5})_{n+1}AlC_n$ and $(Zr,Ti)_{n+1}AlC_n$ exhibited the tendency to be converted to o-MAX phases based on the value of n and the arrangement of the two metal atoms M′ and M″.[64,65] Very recently, solid solution MXene Mo_4VC_4 with five atomic layers was reported to be synthesized from Mo_4VAlC_4 with no other MAX phase impurities.[60] Due to the twinning at the central Mo/V plane, the Mo_4VC_4 indicated a herringbone-type structure and not the typical $P6_3/mmc$ structure of MXenes.

Fig. 2b shows the experimentally synthesized and theoretically predicted non-Ti MXenes, including monometallic and DTM MXenes as of today. All MXenes exhibit unique electrical, magnetic, mechanical, optical, and electrochemical features; thus, equal attention must be paid to all MXenes to uncover the ideal material for a specific application.[66] The following sections discuss the further advantages of non-Ti MXenes.

3. Synthesis methods of non-Ti MXenes

Non-Ti MXenes could typically be synthesized by similar etching methods employed for Ti-based MXenes. The etching of the MAX phase is usually carried out using HF, a mixture of acid and fluoride salt, molten salts, hydrothermal, electrochemical, and Lewis acid methods.[31,67–70] Chemical vapor deposition (CVD), a bottom-up approach, was also used in synthesizing non-Ti MXenes.[71] The type of etchant used greatly influences the surface chemistry and properties of the resultant MXene. Since numerous reviews provide in-depth discussions on the general synthetic route of MXenes, which are also applicable to non-Ti MXenes, herein, the discussions are limited to the critical observations in the synthesis of non-Ti MXenes.

3.1 HF etching method

HF etching is a well-known and widely used method to synthesize MXenes. In a typical synthesis procedure, MAX phases are made to react with particular concentrations of HF at a specific temperature for a specific time duration to transform them into MXenes with –F, –O, and –OH surface terminations.[42,43] The properties of the resultant MXene could be tuned by varying the etching conditions such as the concentration of HF, reaction temperature, and time.[31,50,72] For example, V_2CT_x with a yield of 60% and c lattice parameter (c-LP) of 19.73 Å was obtained by treating V_2AlC with 50% HF for 90 h at room

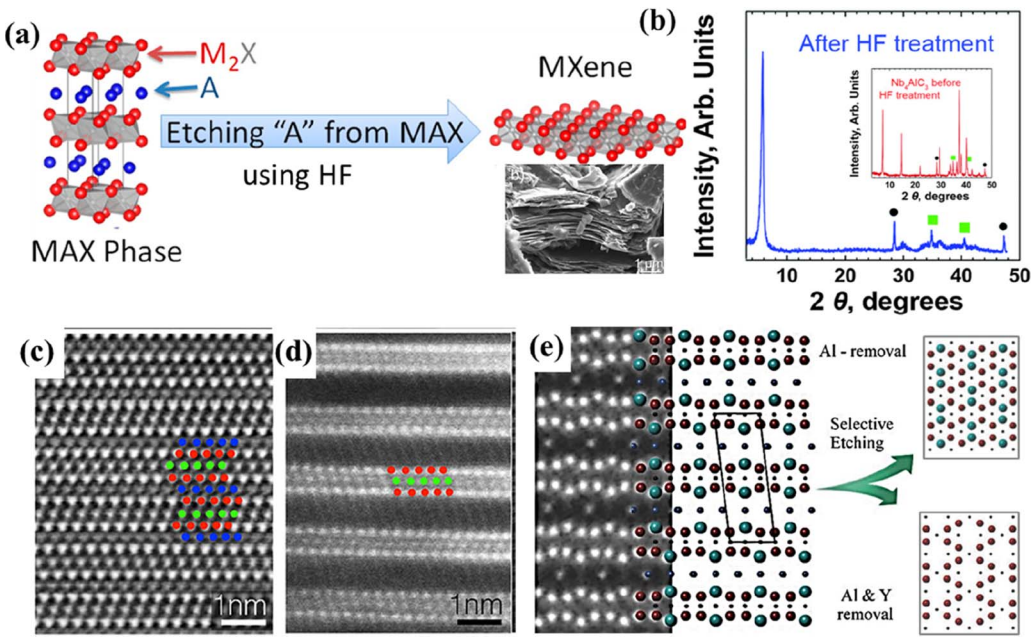

Fig. 3 (a) Schematic illustrating the conversion of MAX to MXene and SEM image of V_2CT_x powders. Reproduced with permission from ref. 31 copyright 2013, American Chemical Society. (b) XRD patterns of Nb_4AlC_3 before (inset) and after HF treatment. Reproduced with permission from ref. 75 copyright 2014, The Royal Society of Chemistry. HRSTEM image of Mo_2TiAlC_2 (c) and $Mo_2TiC_2T_x$ (d) from ref. 48. (e) Structural models representing the two structures obtained based on the etching protocol implemented on $(Mo_{2/3}Y_{1/3})_2AlC$. Reproduced with permission from ref. 50 copyright 2018, Wiley.

temperature (RT).[31] However, the attrition-milled V_2AlC powders subjected to 50% HF for 8 h at RT yielded ~55% V_2CT_x with a *c*-LP of 23.96 Å. This indicates that the *c*-LP of V_2CT_x could be controlled by tuning the etching conditions and the initial particle size. The schematic representation of the conversion of the MAX phase (211) to MXene and the scanning electron microscopy (SEM) image of V_2CT_x powders are shown in Fig. 3a. Very recently, Ghasali *et al.* reported a simple, cost-effective microwave heating method to synthesize the MAX phase V_2AlC and showed that HF etching at higher temperatures led to the formation of delaminated V_2C with fewer defects.[72]

Besides the conventional MAX phases with Al as the A element, the MAX phase Mo_2Ga_2C was used to synthesize Mo_2CT_x MXene using this method.[73] The synthesized multi-layered MXenes can be further delaminated using delaminating agents. The interplanar distance of multi-layered Ta_2C MXene (0.356 nm) was increased to 1.8 nm upon delamination with tetrapropylammonium hydroxide.[74] In contrast to the traditional etching of the MAX phase to produce MXene, $Zr_3C_2T_x$ was obtained by etching Al_3C_2 from a layered ternary material $Zr_3Al_3C_5$, which was synthesized by an *in situ* reactive pulsed electric current sintering (PECS) process.[28] The Al–C layers of the ternary material were weakly bonded and prone to hydrolysis and thus were easily etched by the HF solution. Following the report on the experimental evidence for the existence of $Zr_3C_2T_x$ MXene, Zhou and colleagues first reported the synthesis of $Hf_3C_2T_x$ MXene in 2017.[42] The interfacial bonds in M–C and Al–C layers of the ternary Hf–Al–C were stronger than those in Zr–Al–C; hence, direct exfoliation was difficult. To overcome this issue, the group alloyed Si on the Al sites of $Hf_3Al_4C_6$ to form $Hf_3[Al(Si)]_4C_6$ solid solution, which was later etched with HF to form $Hf_3C_2T_x$. The $Nb_4C_3T_x$ observed as an impurity in the X-ray diffraction (XRD) pattern of Nb_2CT_x was first isolated from its MAX phase by Ghidiu *et al.* in 2014 using aqueous HF.[75] The shift in the (0002) peak towards the left (2θ of 7.23° to 5.77°) in the XRD pattern of $Nb_4C_3T_x$ MXene compared to the XRD of its MAX phase (Fig. 3b) confirmed the formation of $Nb_4C_3T_x$ MXene. The HF etching method was also employed to form other monometallic MXenes, such as $V_4C_3T_x$ and $Ta_4C_3T_x$.[33,43]

Anasori *et al.* first reported the successful synthesis of o-MXenes, $Mo_2TiC_2T_x$, $Mo_2Ti_2C_3T_x$, and $Cr_2TiC_2T_x$, using the HF etching method.[48] From the comparison of the high-resolution scanning transmission electron microscopy (HRSTEM) images of the MAX phase Mo_2TiAlC_2 (Fig. 3c) and the o-MXene $Mo_2TiC_2T_x$ (Fig. 3d), it is evident that HF etched out the Al layers in Mo_2TiAlC_2 to form $Mo_2TiC_2T_x$. Meshkian *et al.* presented the experimental evidence for a new o-MAX phase alloy Mo_2ScAlC_2, from which the o-MXene Mo_2ScC_2 was obtained using HF.[51]

The etching duration and the concentration of HF play a crucial role in obtaining i-MXenes and MXenes with ordered vacancies.[50] The i-MXene $(Mo_{2/3}Y_{1/3})_2C$ was obtained from its MAX phase $(Mo_{2/3}Y_{1/3})_2AlC$ by subjecting the MAX precursors to 48% HF for 12 h. However, different etching conditions, such as 10 wt% HF and 72 h, formed $Mo_{1.33}C$ with a divacancy ordered structure. The schematic representation of the structural models of the MAX and the two different MXenes obtained based on the etching conditions is shown in Fig. 3e. As seen in the scanning transmission electron microscopy (STEM) image (Fig. 3e) of $(Mo_{2/3}Y_{1/3})_2AlC$, the Y atoms were placed out of the Mo plane, closer to the Al atoms due to the difference in the atomic sizes and thus were prone to react with the etchant under strong etching conditions forming divacancy ordered $Mo_{1.33}C$ MXene. The $Mo_{1.33}C$ MXene obtained from the i-MAX phase $(Mo_{2/3}Sc_{1/3})_2AlC$ was similar to the Mo_2C MXene obtained from Mo_2Ga_2C, except for the presence of ordered vacancies at every third Mo atom.[52] The resistivity of the delaminated $Mo_{1.33}C$ was four times less than that of delaminated Mo_2C. Meshkian *et al.* reported the incorporation of tungsten (W) in the stable i-MAX phases $(W_{2/3}Sc_{1/3})_2AlC$ and $(W_{2/3}Y_{1/3})_2AlC$.[76,77] The Al and Sc/Y layers in the i-MAX phases were selectively etched to form $W_{1.33}C$ MXene using HF. The resultant $W_{1.33}C$ MXene obtained from the W–Sc containing i-MAX phase had increased amounts of –OH and –O compared to –F, whereas the $W_{1.33}C$ obtained from the W–Y containing i-MAX phase had equal amounts of terminations.[77]

New MAX phase compounds $(V_{0.5}Cr_{0.5})_3AlC_2$, $(V_{0.5}Cr_{0.5})_4AlC_3$, and $(V_{0.5}Cr_{0.5})_5Al_2C_3$ in the V–Cr–Al–C system were first synthesized by Zhou *et al.* in 2008.[78] Following this, Naguib *et al.* successfully synthesized the M_2C and M_3C solid solution MXenes $(Ti_{0.5},Nb_{0.5})_2C$ and $(V_{0.5},Cr_{0.5})_3C_2$ by immersing MAX phase powders in aqueous solutions of HF.[33] These solid solution MXenes were among the early MXenes reported along with Ti_2C and Ti_3CN by Naguib *et al.* The M_3C_2-based novel solid solution MXene $(Ti_{0.5}V_{0.5})_3C_2$ and Nb-based M_4C_3 solid solution MXenes $(Nb_{0.8},Ti_{0.2})_4C_3T_x$ and $(Nb_{0.8},Zr_{0.2})_4C_3T_x$ were all first synthesized by the HF etching method.[58,59]

The above discussions show that HF etching is the primary method employed to synthesize carbide MXenes. Compared to the experimental conditions employed during the synthesis of Ti-based MXenes with HF etching, a higher concentration of HF and the reaction time were used to synthesize non-Ti MXenes.[79] Although stronger HF etching conditions are reported to lead to increased surface defects and poor-quality Ti-MXenes, this phenomenon was not much reported for non-Ti MXenes.

3.2 Acid–salt etching method

A mixture of acid (HCl/H_2SO_4) and fluoride salt (LiF/NaF/KF) is also used as an etchant to produce MXenes from their MAX phases. The metal cations can be intercalated into the MXene layers and delaminate them without the need for a separate delaminating agent, unlike the HF etching method.[66] Besides the conventional HF etching, V_2CT_x MXene can be synthesized using the LiF–HCl etching method, like their Ti counterparts.[67] The LiF–HCl etching method improved the stability of delaminated V_2C suspended in water. The mildly oxidized V_2CT_x MXene synthesized through a one-pot hydrothermal-assisted LiF–HCl etching method exhibited enhanced storage capabilities in lithium-oxygen batteries than the mildly oxidized $Ti_3C_2T_x$.[80] o-MXenes such as $Cr_2TiC_2T_x$ and solid solution MXenes such as TiVC, $(V_y,Ti_{1-y})_2C$ (y = 1, 0.7, 0.5, 0.3, 0), and $(Ta_{0.38}Ti_{0.62})_3C_2T_x$ have been successfully synthesized by the LiF–HCl etching method.[48,81–83]

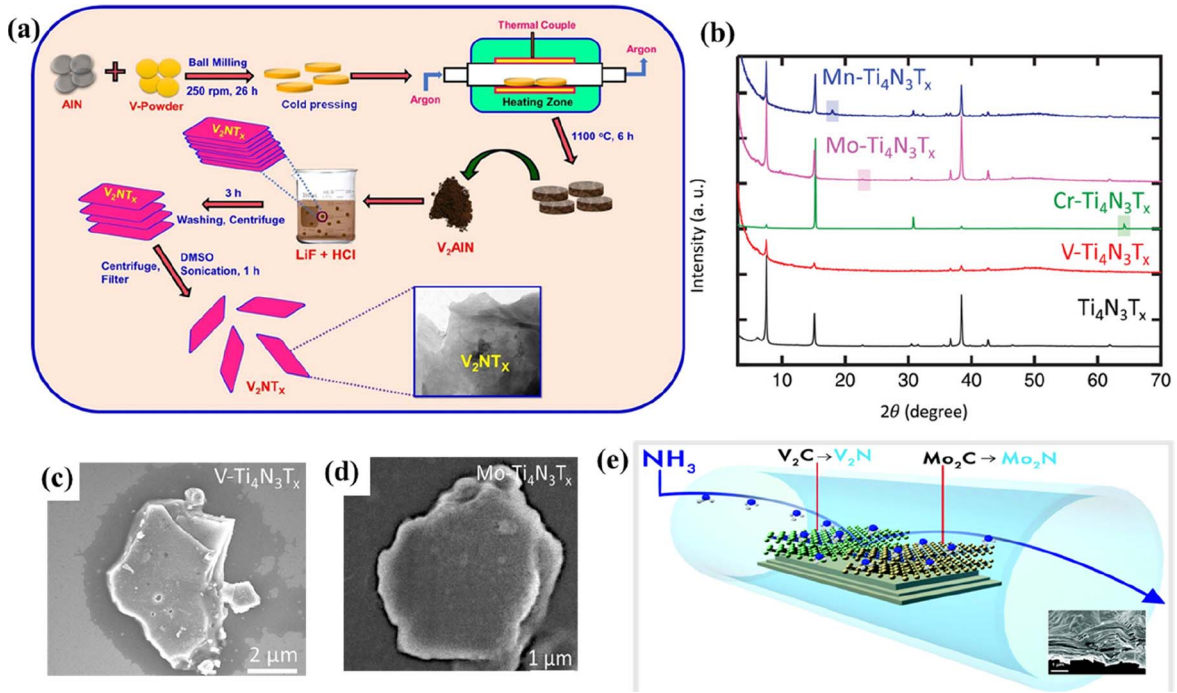

Fig. 4 (a) Process flow indicating the formation of V_2NT_x MXene from ref. 87. (b) X-ray diffraction patterns of exfoliated $Ti_4N_3T_x$ and M–$Ti_4N_3T_x$ (M = V, Cr, Mo, and Mn) MXene, and SEM image of (c) V–$Ti_4N_3T_x$ and (d) Mo–$Ti_4N_3T_x$. Reproduced with permission from ref. 89 copyright 2020, Wiley. (e) Schematic of the synthesis of 2D transition metal nitrides by the ammoniation of carbide MXenes (Mo_2CT_x and V_2CT_x) at elevated temperatures. Reproduced with permission from ref. 91 copyright 2017, Royal Society of Chemistry.

In the formative years of establishing the synthesis protocols for non-carbide MXenes, not enough success was achieved through similar techniques used for carbide MXenes.[84] In most initial cases, MAX phases were directly etched with the use of HF (40–50%), resulting in low-quality MXene layers.[33,84–86] Studies gradually adopted the use of an acid–salt etchant to produce nitrogen-containing MXenes.[87,88] V_2NT_x was the first non-Ti nitride MXene reported by Venkateshalu *et al.* by etching Al layers from V_2AlN using the LiF–HCl acid–salt etching method, as shown in Fig. 4a.[87] However, some Al layers were retained after the acid–salt etching, which was further reduced after the delamination process. V_2NT_x had a stacked morphology and appeared in uneven-sized blocks that were converted into lamellar structures with damaged edges after exfoliating with dimethyl sulfoxide (DMSO). Despite the low toxicity levels compared to the HF etching method, the LiF–HCl method results in incomplete etching of MAX phases. The synthetic conditions must be optimized to tackle the drawback of the LiF–HCl etching method.

3.3 Molten salt and hydrothermal method

As described previously, the molten salt etching method is widely used to synthesize nitride MXenes that are unstable in HF. The MAX phases are treated with an eutectic molten salt mixture (typically LiF + KF + NaF) or Lewis acidic molten salts and washed with concentrated acids to remove the impurities.[69,84] The multi-layered MXenes are further delaminated using delaminating agents.[84] However, the MXenes obtained through this method have increased defects compared to their HF-etched counterparts. Until today, Ti-based MXenes have been the only ones reported to be synthesized by using a eutectic mixture of molten salts. However, the resultant Ti-based MXenes can be modified by adding various metal ions to form mixed transition metal nitride MXenes. Djire *et al.* reported the synthesis of M–$Ti_4N_3T_x$ (M = V, Cr, Mo, or Mn; T = O and/or OH) by modifying the pristine $Ti_4N_3T_x$ MXene with various metal ions.[89] M–$Ti_4N_3T_x$ exhibited similar diffraction patterns resembling those of pristine $Ti_4N_3T_x$, indicating good structural stability (Fig. 4b). The SEM images of the mixed metal nitride MXenes indicated an accordion-like structure with visible open layering (Fig. 4c and d). Kamysbayev *et al.* reported the synthesis of Nb_2CT_x (T = Cl, S, Se, NH) using molten $CdCl_2$.[69] The synthesized MXene showed superconducting behavior strongly influenced by surface terminations.

Hydrothermal synthesis is a facile and environmentally benign method to produce non-Ti MXenes. Peng *et al.* demonstrated a simple and safe hydrothermal etching method to synthesize Nb_2CT_x MXene.[68] Nb_2AlC was mixed with HCl containing $NaBF_4$ and subjected to a hydrothermal reaction. The resultant was washed, filtered, and dried in a vacuum to obtain Nb_2CT_x MXene. Due to the slow release mechanism of the hydrothermal method, the resultant Nb_2CT_x MXene had a higher lattice constant, surface area, and interlayer spacing than its HF-etched counterpart.

3.4 Other notable methods

Besides the commonly used techniques to synthesize non-Ti MXenes discussed above, various other notable etching methods, such as UV-induced, algae extraction, ammoniation,

electrochemical, and CVD, have also been successfully implemented.[40,70,71,90,91] Zada *et al.* reported a green method to synthesize V_2C MXene.[90] The MAX phase V_2AlC was intercalated and delaminated using algae extraction to produce V_2C nanosheets. The V_2C MXene prepared by this method exhibited higher antibacterial ability than Ti_3C_2.[38] Mei *et al.* reported a UV-induced etching strategy to produce Mo_2CT_x MXenes.[40] Mo_2Ga_2C was mixed with phosphoric acid and stirred continuously under the irradiation of UV. The solution was centrifuged, filtered, and dried to obtain Mo_2C powder. Mo_2C synthesized from Mo_2Ga_2C through the safe UV-induced selective etching method exhibited a graphene-like morphology with high purity.

A CVD approach was also reported to grow 2D ultrathin α-Mo_2C crystals with lateral sizes of over 100 μm.[71] Methane was used as a carbon source, and Cu foil above Mo foil was used as the substrate. At a high growth temperature of 1085 °C, the Cu melted, forming a Mo–Cu alloy at the liquid interface of Cu/Mo. With subsequent heating, the Mo atoms occupied the surface of liquid Cu and reacted with the carbon atoms to form α-Mo_2C crystals. The ultrathin 2D α-Mo_2C obtained through the CVD method was of very high quality. The bottom-up approaches for synthesizing MXenes are not widely used like the top-down approaches due to the complicated procedures. Considering the quality of MXenes obtained from these methods, researchers must focus more on the bottom-up approaches for mass production of MXenes. Pang *et al.* reported a thermal-assisted electrochemical etching technique to synthesize Cr_2CT_x and V_2CT_x MXenes.[70] The substrate drives the morphology of the electrochemically etched MXene flakes. Furthermore, 3D MXene composites could be easily formed with this method.

Ammoniation is a prominent technique to produce nitride MXenes from carbide MXenes. Mo_2NT_x MXene was synthesized for the first time by Urbankowski *et al.* by substituting the C atoms in Mo_2CT_x MXene with N atoms through ammoniation, as shown in Fig. 4e.[91] Using the same method, they also demonstrated the successful synthesis of V_2N MXene from V_2CT_x MXene. The heat treatment of Mo_2CT_x and V_2CT_x MXenes in the presence of ammonia at about 800 °C resulted in their transformation to Mo_2N, V_2N, and VN MXenes. As the ammoniation reaction temperature was increased from 400 °C to 600 °C, the ratio of N to C atoms increased significantly. Mo_2N had a distorted hexagonal structure, while V_2N and VN had respective trigonal and cubic structures with the basal plane of $P6_3/mmc$ symmetry similar to their carbide precursors. Very recently, Gao *et al.* synthesized Mo-based nitride MXenes using a similar atomic substitution approach described by Urbankowski *et al.*[92] MoS_2 was subjected to nitridation by introducing ammonia into a horizontal quartz tube furnace at about 700 °C. MXenes with different phases of Mo–N (Mo_5N_6 and δ-MoN) were synthesized by controlling the reaction temperature and time.

As mentioned earlier, the growth of non-Ti MXenes is anticipated to be hindered due to the great challenges in their synthesis. However, upon analyzing the reported syntheses techniques, it is obvious that the non-Ti MXenes can adopt similar techniques to their Ti counterparts, resulting in similar structures. From the myriad synthetic options for non-Ti MXenes, it can be deduced that investing more efforts in optimizing the synthesis conditions to produce high-quality, stable non-Ti MXenes would be very fruitful.

4. Properties of non-Ti MXenes

While enormous research focus has been placed on Ti-based MXenes, the research efforts are very feeble on non-Ti MXenes despite their potentially useful properties. In an attempt to encourage researchers to focus on the extended family of MXenes, the intriguing properties exhibited by non-Ti MXenes are provided in this section. The properties determined experimentally and predicted theoretically are discussed for an in-depth analysis of their electronic, magnetic, optical, and mechanical properties. Furthermore, the properties of non-Ti MXenes are compared with Ti MXenes.

4.1 Electronic properties

The electronic properties of non-Ti MXenes vary based on the composition, surface terminations, temperature, strain, molar volume, *etc.* With bands across the Fermi level in the electronic band structure (Fig. 5a), pristine V_2C MXene was metallic in nature.[80] Highly influenced by doping, molar volume, and temperature, Mo_2C MXene was predicted to have electrical and thermal conductivities of 106 Ω^{-1} m^{-1} and 48.4 W m^{-1} K^{-1}, respectively.[93] The electronic properties of Mo_2C MXene can be further altered by modulating its phase, biaxial strain, and surface functionalities.[94] The O terminations were preferred on 2H-MoC_2, making it a topological insulator. In contrast, the Cl atoms preferred to be terminated on 1T-MoC_2, which changed from semi-conducting to metallic upon increasing the strain beyond 5%. The type of etching method used to synthesize MXenes also influenced their properties. For example, the Nb_2CCl_x synthesized using the molten salt $CdCl_2$ showed the characteristics of a typical type-II superconductor with a critical temperature (T_c) ~ 5.2 K.[69] In contrast, the Nb_2CF_x synthesized through the hydrothermal assisted LiF–HCl etching method was dynamically unstable and was not superconducting.[95] The electron/hole/N-doping changed the electronic properties of the MXene, whereas the magnetic properties remained unchanged.[96] However, metal doping could change the electronic as well as the magnetic properties of the system. With excellent hydrophilicity, variable valence states (+2, +3, and +4), high surface area (31.35 m^2 g^{-1}), electrical conductivity (1137 S m^{-1}), and large pore volume (~0.047 cm^3 g^{-1}), $V_4C_3T_x$ MXenes were constantly explored in various energy storage and conversion systems.[97–99] The large interlayer spacing of ~0.466 nm, larger than that of Ti and Mo containing MXenes, makes them suitable for energy applications.[97]

Like V_2C MXenes, the theoretical results for the electronic density of states showed that V_2NT_2 (T = O, F, OH, and S) MXenes were highly conductive, with most electron states at the Fermi level originating from the V 4d orbitals.[100] This metallic nature of V_2NT_2 is beneficial to electron transfer reactions, and V_2NT_2 is predicted to be a promising host material for energy

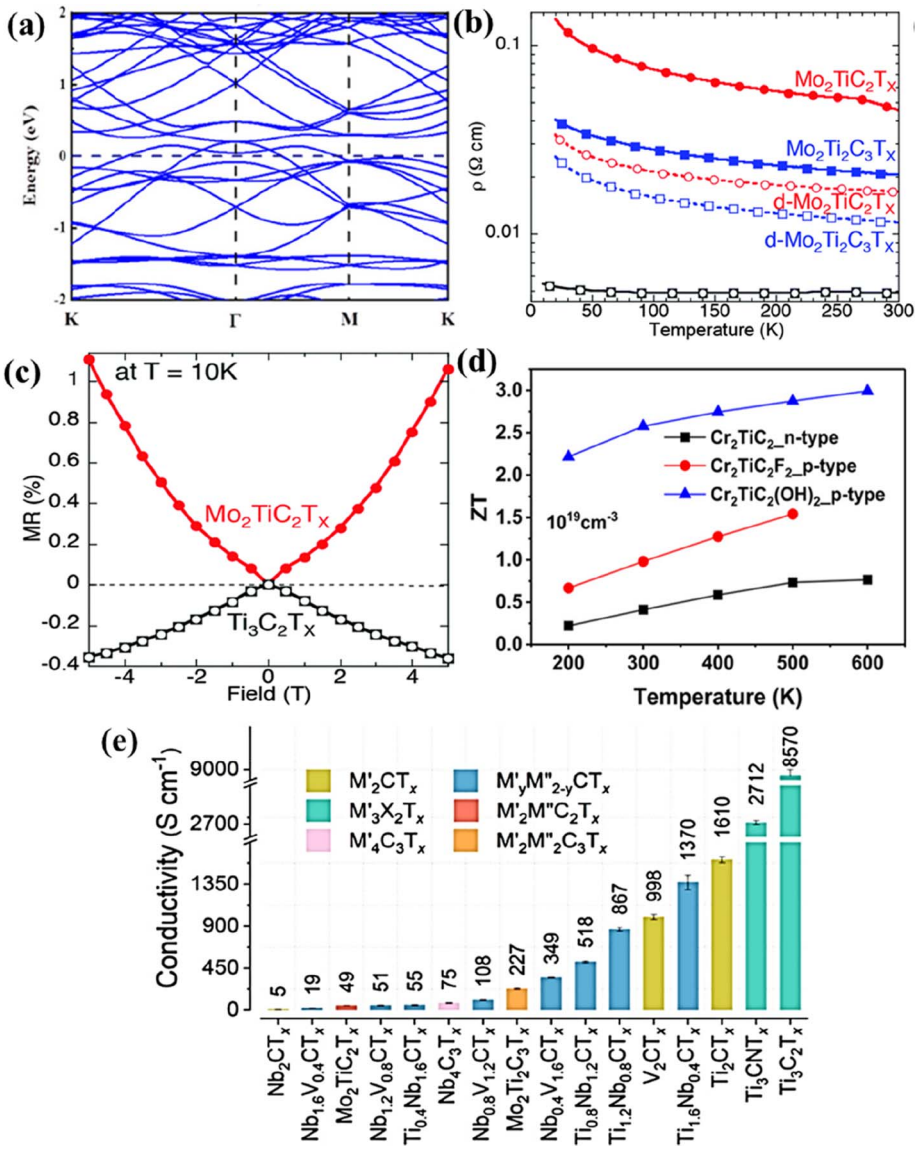

Fig. 5 (a) Electronic band structures of V_2C. Reproduced with permission from ref. 80 copyright 2021, American Chemical Society. (b) Temperature dependence of the resistivity for a $Mo_2TiC_2T_x$ (red), $Mo_2Ti_2C_3T_x$ (blue), and $Ti_3C_2T_x$ (black) and (c) the corresponding magnetic field dependent magnetoresistance taken at 10 K. Reproduced with permission from ref. 57 copyright 2016, Royal Society of Chemistry. (d) Thermoelectric figure of merit (*ZT*) for Cr_2TiC_2 and $Cr_2TiC_2T_2$ (T = −F and −OH) between 200 and 600 K. Reproduced with permission from ref. 101 copyright 2019, American Chemical Society. (e) The electrical conductivity of different vacuum-filtered MXene films. Reproduced with permission from ref. 102 copyright 2020, American Chemical Society.

storage devices. The transformation of carbide MXenes Mo_2CT_x and V_2CT_x to their respective nitride counterparts, Mo_2NT_x and V_2NT_x, through the ammoniation method was accompanied by a change in electronic properties.[91] The electronic structure of the MXenes changed from semi-conducting to metallic, leading to decreased resistivity values of the nitride MXenes. The room temperature resistivity values of pristine Mo_2CT_x and Mo_2NT_x were determined to be 3.6×10^{-1} and 4.8×10^{-4} Ω cm, respectively. For the vanadium-based MXenes, the resistivity values of pristine V_2CT_x and V_2NT_x were calculated to be 2.6×10^{-3} and 2.4×10^{-4} Ω cm, respectively. Therefore, it can be summarized that V_2NT_x and Mo_2NT_x have better conductivities than their carbide counterparts. Furthermore, different phases of Mo–N MXenes (Mo_5N_6 and δ-MoN) produced by controlling the reaction temperature and time also have different electronic properties.[92] Among both phases, Mo_5N_6 had lower conductivity than δ-MoN due to the less availability of free electron concentration throughout the crystal. δ-MoN had an electrical conductivity of 3126 S cm^{-1}, comparable to that of $Ti_3C_2T_x$ (3092–6450 S cm^{-1}).

The electronic properties of DTM MXenes are influenced by the stoichiometric ratio of the two metals, temperature, and thickness of the MXene layers. DC transport measurements showed that the $Ti_3C_2T_x$ MXene was metallic in the temperature range from 130–250 K, and at temperatures below 130 K, its resistivity increased.[57] However, the resistivity of o-MXenes,

$Mo_2TiC_2T_x$ and $Mo_2Ti_2C_3T_x$ increased below 250 K (Fig. 5b). Similarly, the magnetoresistance measurements of $Ti_3C_2T_x$ and Mo–Ti containing o-MXenes at 10 K shown in Fig. 5c had opposite signs indicating different transport properties. Temperature-dependent conductivity and magnetoresistance measurements indicated the semiconductor-like and metallic behavior of Mo–Ti and $Ti_3C_2T_x$ MXenes, respectively. Furthermore, density functional theory (DFT) calculations suggested that by changing the outermost layers of $Ti_3C_2(OH)_2$ by Mo, the resultant $Mo_2TiC_2(OH)_2$ could exhibit semiconductor-like electronic properties. This approach to changing the electronic properties of MXenes by tuning the outermost transition metal layers is much simpler than other methods, such as altering the phase, surface termination, and doping. Cr_2TiC_2 and $Cr_2TiC_2T_2$ (T = –F and –OH) o-MXenes are predicted to be moderate band gap semiconductors and efficient thermoelectric materials with a high dimensionless figure of merit (*ZT*).[101] Specifically, the p-type $Cr_2TiC_2(OH)_2$ was predicted to have a *ZT* value of 3.0 at 600 K with a thermoelectric efficiency of 20%. The thermoelectric *ZT* and conversion efficiency of Cr–Ti containing o-MXenes are shown in Fig. 5d.

The cold-pressed free-standing discs of $(Ti_{0.5},Nb_{0.5})_2AlC$ had a sheet resistivity and a contact angle for water droplets of 0.052 $\Omega\ m^{-1}$ and 31°, respectively, which were less than those of Ti_2C (0.068 $\Omega\ m^{-1}$ and 32°, respectively).[33] It was hypothesized that the high resistivity of Mo_4VC_4 (1.20 mΩ cm) as compared to thinner Mo-based MXenes such as Mo_2C (0.80 mΩ cm) and Mo_2TiC_2 (0.67 mΩ cm) could be due to the increased thickness of Mo_4VC_4 with poor stacking and interflake resistivity.[60] Furthermore, as mentioned earlier, the properties of solid solution MXenes could be tuned by varying the stoichiometric ratio of the two metals. For example, the electrical conductivity of $Ti_yNb_{2-y}CT_x$ and $Nb_yV_{2-y}CT_x$ ($y = 0.4$, 0.8, 1.2, and 1.6) could be altered by varying the ratio $M' : M''$.[102] As seen in Fig. 5e, $Ti_{0.4}Nb_{1.6}CT_x$ had a conductivity of 55 S cm^{-1}, whereas $Ti_{1.6}Nb_{0.4}CT_x$ had an increased conductivity of 1370 S cm^{-1}. Similarly, Pinto *et al.* reported that the electrical properties of the newly synthesized $Mo_yV_{4-y}C_3$ (x= 1, 1.5, 2, and 2.7) could be tuned by altering the ratios of the metals (Mo : V) and the surface terminations (O : F).[103] With the decrease in the Mo content of the solid solution MXene $Mo_yV_{4-y}C_3$, its resistivity increased (Fig. 6a). The solid solution MXene composition with the highest Mo content $Mo_{2.7}V_{1.3}C_3$ exhibited an excellent electrical conductivity of 830 S cm^{-1}. Furthermore, they reported that with different quantities of –O terminations from the –F terminations, MXenes could exhibit positive values of magnetoresistance (Fig. 6b).

Since the electronic properties of MXenes largely depend on their composition, tuning the composition of MXenes to achieve the desired conductivity is imperative. Furthermore, the etching conditions should also be carefully controlled as MXenes with fewer defects and large lateral sizes exhibit higher electronic properties.

4.2 Magnetic properties

The non-Ti MXenes are predicted to possess magnetic moments like their Ti counterparts. Like the Ti MXenes, the properties and performance of the non-Ti MXene could also be optimized through the surface terminations (–O/–F/–OH/–S).[104–107] The

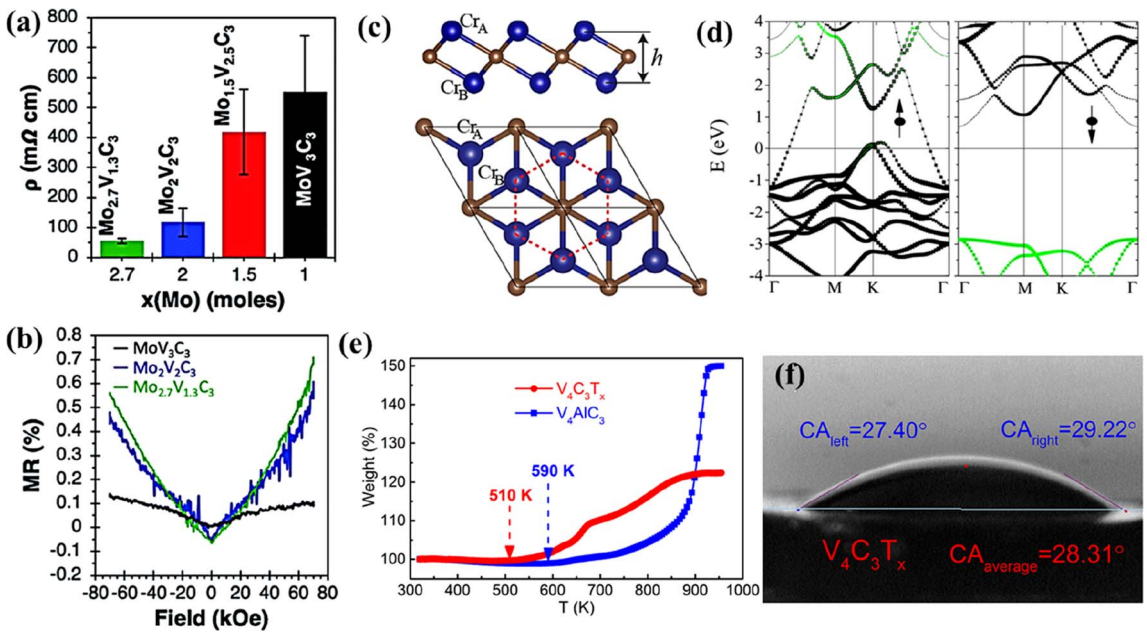

Fig. 6 (a) Resistivity and (b) magnetoresistance of the $Mo_xV_{4-x}C_3$ multilayer. Reproduced with permission from ref. 103 copyright 2020, Royal Society of Chemistry. (c) Side and top views of the Cr_2C MXene lattice (blue and brown balls represent Cr and C atoms, respectively) and (d) band structure for Cr_2C MXene. Reproduced with permission from ref. 114 copyright 2015, American Chemical Society. (e) Thermogravimetric curves of V_4AlC_3 and $V_4C_3T_x$ between 320 and 960 K in air and (f) photograph of the water droplet shape with the contact angle on cold-pressed free-standing discs of $V_4C_3T_x$. Reproduced with permission from ref. 97 copyright 2019, Elsevier Ltd.

non-Ti MXenes were doped/intercalated and formed composites with other materials to modulate their properties.[108,109] V_2CT_x exhibited intrinsic ferromagnetism with a magnetic moment of 0.013 emu g^{-1}, which is close to the values reported for La-doped Ti_3C_2,[110] thus exhibiting the potential to be used in spintronic applications.[111] Using DFT computations, Luo *et al.* predicted the magnetic moment of Zr_3C_2 MXene and Hf_3C_2 MXenes as 1.69 μ_B per cell and 1.40 μ_B per cell, respectively.[112] Using DFT, Gao *et al.* predicted that magnetism could be imparted to i-MXenes by alloying magnetic transition metal atoms with nonmagnetic MXenes.[113] Furthermore, they reported that the magnetic ground state and anisotropy could be tuned using strain. They also predicted that i-MXenes could be used as antiferromagnetic topological insulators and spin-gapless semiconductors. Cr_2C is the first reported half-metallic ferromagnet among the members of the MXene family predicted to be obtained by etching its MAX phase Cr_2AlC.[114] The lattice structure of Cr_2C shown in Fig. 6c depicts the arrangement of Cr in hexagonal structures with the C atoms of two different layers forming two triangular sublattices. Through hybrid DFT, it was predicted that the itinerant Cr d electrons spin-polarized around the Fermi surface (Fig. 6d) induce ferromagnetism which in turn introduces half-metallicity with a gap of 2.85 eV in the Cr_2C MXene. By terminating the surface of Cr_2C with functional groups (–F, –OH, –H, or –Cl), the MXene was predicted to change from a metal to an insulator and ferromagnetic to antiferromagnetic. Furthermore, it was determined that the type of surface functionalization controlled the energy gap of the antiferromagnetic insulating state.

Cr_2C and Cr_2N are predicted to be ferromagnetic, while Ti_3C_2 and Ti_3N_2 are antiferromagnetic.[29,37] The ferromagnetic nature of Mn_2NT_x is not influenced by the surface terminations; however, Ti_3CNT_x and $Ti_4C_3T_x$ become non-magnetic in the presence of surface terminations.[115] This change in the magnetic properties with varying MXene composition further stresses the importance of exploring non-Ti MXenes.

4.3 Optical properties

The variable composition and 2D morphology impart unique optical features to MXenes. With larger nonlinear absorption coefficients and refractive indices than the representative $Ti_3C_2T_x$, the V_2C MXene could be used to implement high-performance photonic devices at 1.9 μm wavelength.[116] With an optical band gap of 0.81 eV, Nb_2CT_x exhibited ultrafast carrier dynamics and broadband nonlinear optical response suitable for nanophotonic devices.[117,118] With superior photothermal conversion efficiency, Nb_2C-supported Ni nanoparticles were efficient photothermal catalysts for CO_2 with a conversation rate (8.50 mol g_{Ni}^{-1} h^{-1}) much higher than that of the Ni/Ti_3C_2 composite (702.4 mmol g_{Ni}^{-1} h^{-1}).[39] The surface terminations influenced the optical properties of the $Ta_4C_3T_x$ MXene.[119] In the infrared region, the O-terminated Ta_4C_3 had greater absorption coefficients and reflectivity than pristine Ta_4C_3. In the visible region, the Ta_4C_3 monolayer exhibited a selective transmittance of 35% at 1.65 eV and 84% at 2.25 eV.[120] This highly responsive nature of $Ta_4C_3T_x$ to visible light is beneficial for optical detection. From the visible to near-infrared region (400 to 2500 nm), Mo_4VC_4 exhibited a featureless absorption spectrum indicating its potential applications as transparent conducting electrodes. Although numerous optical features are predicted and reported for non-Ti MXenes, an in-depth elucidation on the same is necessary for their practical applications.

4.4 Mechanical properties

With strong M–X bonds, MXenes exhibit excellent mechanical properties. The mechanical properties of MXenes influence the electrochemical performance of flexible electrodes. The non-Ti MXenes are reported to exhibit higher structural stability and Young's modulus than the Ti MXenes.[28,121] The mechanical properties of the non-Ti MXenes have been evaluated experimentally and theoretically and are affected by the composition, functional groups, strain, stress, and thickness of the MXene layers. An elastic modulus of 312 ± 10 GPa was predicted for Mo_2CT_x MXene under biaxial strains.[93] The biaxial strain and surface functional groups can tune the properties of the M_2C MXene.[94] O-terminated Zr_3C_2 presented a mechanical strength of 392.9 GPa.[28] With higher binding energy, the $Zr_3C_2T_x$ MXene exhibited better structural stability than $Ti_3C_2T_x$. Using DFT computations, Luo *et al.* predicted the elastic constants, Young's Modulus, free energy, and work function of Zr_3C_2 MXene as 246 (C_{11}), 230 N m^{-1}, −7.431 E, and 3.996 eV, respectively.[112] $Nb_4C_3T_x$ MXenes exhibited higher in-plane stiffness (600 N m^{-1}) compared to other MXenes and 2D materials such as $Ti_3C_2O_2$(361 N m^{-1}), Ti_2C (135 N m^{-1}), graphene (335 N m^{-1}), h-BN (267 N m^{-1}), α-boron monolayers (225 N m^{-1}), silicene (63 N m^{-1}) and phosphorene (88 N m^{-1}).[122] The Young's modulus of the monolayer $Nb_4C_3T_x$ membrane calculated from AFM nanoindentation was 386 ± 13 GPa, which was the highest among the 2D materials such as graphene and $Ti_3C_2T_x$.[121] The $V_4C_3T_x$ MXene exhibited high thermal stability in air (510 K), as shown in Fig. 6e, and enhanced hydrophilicity with a contact angle of 28.31° (Fig. 6f), which was much lower than those reported for Ti_2CT_x (32°), $Ti_3C_2T_x$ (34°), and $Ta_4C_3T_x$ (41°) MXenes.[97] The properties of the $Ta_4C_3T_x$ MXene could be enhanced by engineering the interlayer distance.[123] When 2D MoS_2 was placed in the interlayers of 2D Ta_4C_3, the interlayer spacing of the resultant composite (MoS_2–Ta_4C_3) was increased to 1.69 nm from 1.55 nm (Ta_4C_3). This increase in the interlayer spacing improved the conductivity of the Ta_4C_3 matrix, prevented its aggregation, and optimized the structural stability.

From the above discussions, it is evident that the mechanical properties of non-Ti MXenes vary with their composition. However, research should be carried out to evaluate the effect of surface terminations on the mechanical properties of non-Ti MXenes. Furthermore, experiments should be carefully designed to tailor the morphology and composition of non-Ti MXenes to obtain mechanical properties advantageous for practical applications.

5. Applications of non-Ti MXenes

With rich surface chemistry, tunable composition, good electrical conductivity, flexible 2D morphology, and chemical stability, non-Ti MXenes are suitable for various applications. This section discusses the energy-related applications of non-Ti MXenes in batteries, supercapacitors, electrocatalysis, and other notable fields.[102,117,124–128] Furthermore, the performance of non-Ti MXenes is compared with that of Ti MXenes to highlight the necessity to study all the members of the MXene family. The applications of non-Ti MXenes are summarized in Table 1. Besides providing a brief overview of the applications of non-Ti MXenes, the section also outlines their current challenges to motivate further research.

5.1 Batteries

The non-Ti MXenes exhibit electrochemical properties conducive to battery applications like their Ti-containing counterparts. With enhanced electronic conductivity, ion mobility, storage capacity, and decreased open circuit voltage, the non-Ti MXenes can outperform the Ti-based MXenes, when used as battery electrodes.[129] Recently, Firestein *et al.* reported that electrochemically activated delaminated V_2C MXene exhibited excellent performance as a cathode for aqueous zinc-ion batteries (ZIBs).[67] It was shown that the charge storage mechanism of delaminated V_2C MXene could be tuned with different activation processes. As discussed in the previous section, the functional groups (–O, –F, and –OH) created on the surface of the multilayered MXene help in

Table 1 Summary of applications of non-Ti MXenes and performance comparison with Ti-based MXenes

Material	Etchant	Application	Performance	Ref.
Nb_2CT_x/CNT	LiF + HCl	Li-ion battery	400 mA h g^{-1} at 0.5C	134
MoS_2–Ta_4C_3	40% HF	Na-ion battery	218.8 mA h g^{-1} at 0.1 A g^{-1}	123
V_2CO_2	HF	Li–O_2 battery	8577.3 mA h g^{-1} at 0.1 A g^{-1}	104
$Mo_2TiC_2T_x$	48–51% HF	Li-ion battery	176 mA h g^{-1} at 1C	48
$Hf_3C_2T_z$	35% HF	Na-ion battery	137 mA h g^{-1} at 0.2 A g^{-1}	42
$Nb_4C_3T_x$	49% HF	Li-ion battery	380 mA h g^{-1} at 0.1 A g^{-1} after 100 cycles	131
V_4C_3	40% HF	Li-ion storage	225 mA h g^{-1} at 0.1 A g^{-1} after 300 cycles	98
$(Nb_{0.8},Ti_{0.2})_4C_3T_x$ and $(Nb_{0.8},Zr_{0.2})_4C_3T_x$	50% HF	Li storage	158 and 132 mA h g^{-1} after 20 cycles	59
Ti_3C_2	49% HF	Li-ion storage	123.6 mA h g^{-1} at 1C	135
$Ti_2C_{0.5}N_{0.5}T_x$	KF + HCl	Na-ion battery	182 mA h g^{-1} at 20 mA g^{-1}	36
Ti_3CNT_x	HF etching	K-ion battery	90 mA h g^{-1} at 10 mA g^{-1}	136
$Ta_4C_3T_x$-TTO	(HCl/KOH)	Supercapacitor	194 F g^{-1} at 1 mV s^{-1}	137
Ta_4C_3	HF	Supercapacitor	481 F g^{-1} at 5 mV s^{-1}	138
$V_4C_3T_x$	49% HF	Supercapacitor	292 F g^{-1} at 2 mV s^{-1}	125
V_4C_3	40% HF	Supercapacitor	209 F g^{-1} at 2 mV s^{-1}	97
$(Mo_{2/3},Y_{(1-x)/3})_2C$	48% HF	Supercapacitor	230 F g^{-1} at 20 mV s^{-1}	50
$W_{1.33}CT_x$	48% HF	Supercapacitor	191 F g^{-1} at 20 mV s^{-1}	77
$Mo_{1.33}C$	48% HF	Supercapacitor	339 F g^{-1} at 2 mV s^{-1}	52
V_2NT_x	LiF + HCl	Supercapacitor	112.8 F g^{-1} at 1.85 mA cm^{-2}	87
$Mo_2TiC_2T_x$	48–51% HF	Supercapacitor	413 F g^{-1} at 2 mV s^{-1}	48
Ti_3C_2	40% HF	Supercapacitor	283 F g^{-1} at 0.5 A g^{-1}	24
Ti_2C	LiF + HCl	Supercapacitor	382 F g^{-1} at 2 mV s^{-1}	139
Ti_2NT_x	O-assisted molten salt etching	Supercapacitor	201 F g^{-1} at 2 mV s^{-1}	140
Ti_3CNT_x	LiF–HCl etching	Supercapacitor	376 F g^{-1} at 10 mV s^{-1}	141
Mo_2CT_x	10% HF	HER	305 mV at 10 mA cm^{-2}	142
Pd/Nb_2CT_x	40% HF	HER	34 mV at 10 mA cm^{-2}	143
$Ni@V_4C_3T_x$	HF	HER	356.6 mV at 10 mA cm^{-2}	126
$MOOH@V_4C_3T_x$	HF	OER	275.2 mV at 10 mA cm^{-2}	99
$Ni@V_4C_3T_x$	HF	NRR	21.29 μg h^{-1} mg_{cat}^{-1} at 0.2 mA cm^{-2}	126
NbTiC	48% HF	H_2 storage	Hydrogen capacity of 6.8 wt%	144
Ti_3C_2/MoS_x	LiF–HCl	HER	196 mV at 50 mA cm^{-2}	145
Ti_3CNT_x	HF etching	HER	148 mV at 10 mA cm^{-2}	146
$Ti_4N_3T_x$	O-assisted molten salt etching	HER	625 mV at 10 mA cm^{-2}	89
$V_4C_3T_x$	HF	Acetone sensor	Detection limit of 1 ppm	127
Mo_2C/CdS	40% HF	Photocatalytic H_2 production	H_2 production rate of 17 964 mol g h^{-1}	147
Nb_2C	Hydrothermal	Dye degradation	Faster dye degradation than Ti_3C_2	68
Nb_2C	40% HF	Nanophotonics	Reverse saturable absorption at 1500–1600 nm	117

tuning the properties of MXenes.[104,124] As O terminations have a strong affinity towards LiO_2 and Li_2O_2, large amounts of O-terminations on the MXene surface could improve the cycling stability of Li–O_2 batteries.[104]

Xu *et al.* reported that the F and OH-terminations in V_2CT_x could be removed through freeze-drying and annealing at 400 °C to obtain V_2CO_2 MXene, which exhibited high capacity and cycling stability of 302 cycles when used as a Li–O_2 battery electrode.[104] The mildly oxidized (mo) V_2CT_x delivered a specific capacity (22 752 mA h g^{-1}) 1.6 times higher than that of mo-$Ti_3C_2T_x$ (14 378 mA h g^{-1}) and a charge transfer resistance (37.3 Ω) lower than that of mo-$Ti_3C_2T_x$ (62.9 Ω) when employed as a Li–O_2 battery electrode (Fig. 7a).[80]

The role of O and S-terminations in enhancing the storage performance of V_2C MXene when employed as an anode in the potassium-ion battery (KIB) was theoretically determined using first-principles calculations.[105] The V_2CO_2 and V_2CS_2 MXenes had low diffusion barriers of 0.097 eV and 0.062 eV and theoretical specific capacities of 489.93 mA h g^{-1} and 200.24 mA h g^{-1}, respectively. The specific capacities exhibited by V_2CO_2 and V_2CS_2 were higher than that of Ti_3C_2 (191.8 mA h g^{-1}) and Ti_2CS_2 (416.33 mA h g^{-1}). Prelithiated V_2C

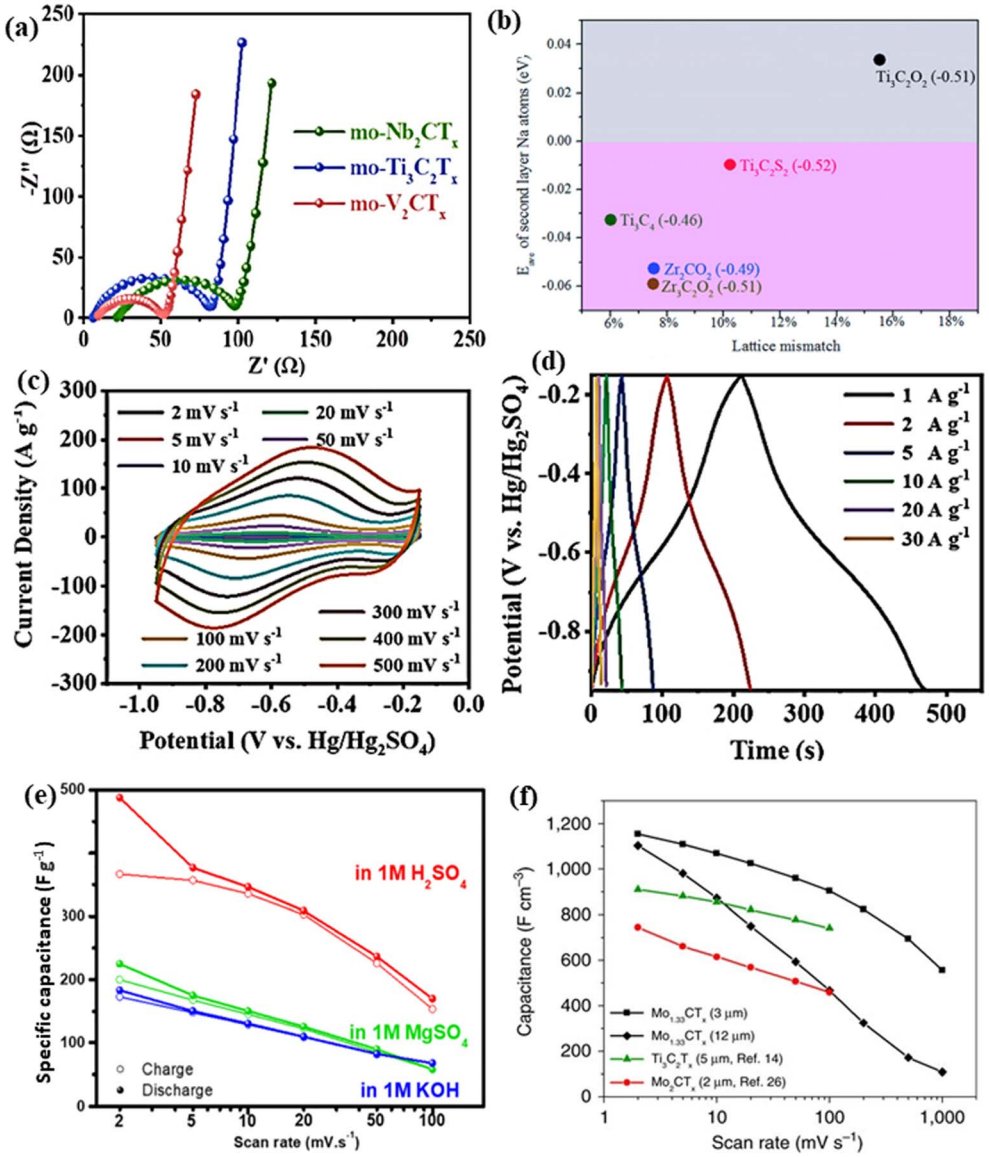

Fig. 7 (a) Nyquist plots at 100 mA g^{-1} of lithium oxygen batteries with mo-MXenes. Reproduced with permission from ref. 80 copyright 2021, American Chemical Society. (b) Comparison of the average adsorption energy of full second layer Na atoms on various MXene-based electrode materials by lattice mismatch and charge transfer values. Reproduced with permission from ref. 129 copyright 2018, Royal Society of Chemistry. (c and d) Electrochemical performance of the delaminated d-$V_4C_3T_x$ film electrode. Reproduced with permission from ref. 125 copyright 2022, Wiley. (e) Specific capacitance of the V_2C electrode measured in different electrolyte media. Reproduced with permission from ref. 149 copyright 2018, Elsevier Ltd. (f) Specific capacitance of 3 and 12 μm thick $Mo_{1.33}C$ free-standing electrodes obtained through three-electrode Swagelok cell measurements from ref. 52.

MXene was reported to be an excellent electrode material for lithium-ion and hybrid magnesium/lithium-ion batteries.[124] V_2C MXene is the only MXene besides Ti_3C_2 to be used as a cathode in hybrid magnesium/lithium-ion batteries with improved co-storage of Li^+ and Mg^{2+} ions. With smaller lattice mismatch and charge transfer values compared to $Ti_3C_2O_2$ and $Ti_3C_2S_2$ MXenes, zirconium carbide MXenes were predicted to be a promising anode material for Na-ion batteries (Fig. 7b).[129] Very recently, it was shown that $Zr_3C_2O_2$ has sodium storage capabilities comparable to $Ti_3C_2O_2$ and higher than $Zr_3C_2T_2$ (T = F, OH, S).[130]

Combined with excellent conductivity, the increased interlayer distance in $Nb_4C_3T_x$ with Li insertion during cycling enabled them to exhibit superior storage performance compared to titanium-based anodes.[131] $Hf_3C_2T_x$ was predicted to be a viable storage material with good conductivity, high structural stability, low diffusion energy barrier, and low open circuit voltage.[132,133] Zhou *et al.* reported that the increased exposure of electrochemically active sites during cycling increased the capacity of $Hf_3C_2T_x$ MXene with increasing cycles when tested as battery electrodes.[42] Besides monometallic MXenes, DTM MXenes were also reported to be potential battery electrodes.[48,82] Wang *et al.* reported that the introduction of another element in the M site of V_2C or Ti_2C MXenes led to the formation of solid solution MXene $(V_x,Ti_{1-x})_2C$ whose electrochemical performance was far superior to that of their monometallic counterparts.[82]

Besides the transition metal and carbon/nitrogen, the functional group also plays a major role in modifying the electrochemical properties of non-Ti MXenes.[104,105] Furthermore, surface defects also influence the Li^+ adsorption capability.[148] Thus, synthesizing non-Ti MXenes with optimized composition remains challenging. During the electrochemical testing of non-Ti electrodes, the electrocatalytic processes should be effectively suppressed to increase the voltage window, cycle life, and energy stored. The newly added members of the MXene family, DTM MXenes possessing excellent properties, should also be tested for energy storage applications.

5.2 Supercapacitors

The high electronic conductivities, large specific surface areas, tunable interlayer spacing, and surface terminations of non-Ti MXenes enable them to be potential electrodes for supercapacitors.[103,149,150] Along with these, the variable valence states of vanadium (+2, +3, and +4), high pore volumes, and good hydrophilicity contributed to the improved electrochemical performance of vanadium carbide (V_4C_3) MXene.[97,125] The delaminated $V_4C_3T_x$ film exhibited a surface capacitive control mechanism with dominant pseudocapacitance.[125] The reversible redox reaction at the surface was evident from the large redox peaks in the cyclic voltammetry curves and the distorted triangular-shaped charge–discharge curves, as shown in Fig. 7c and d. Furthermore, the large interlayer spacing (2.1 nm) of the d-$V_4C_3T_x$ film promoted efficient intercalation and deintercalation of ions without destroying the layered structure resulting in enhanced electrochemical performance. V_2C MXene provided different electrochemical behavior when tested as a supercapacitor electrode in three different electrolytes *viz.* 1 M H_2SO_4, 1 M KOH, and 1 M $MgSO_4$.[149] V_2C showed comparable storage performance to Ti_3C_2 in all the electrolytes, with its best in 1 M H_2SO_4 (487 F g^{-1} at 2 mV s^{-1}), as shown in Fig. 7e. The performance difference in various electrolytes was attributed to the changes in conductivity, ion size, desolvation energy, and charge on the cation.

Like Ti_3C_2, the V_2NT_x MXene has also exhibited the potential to be used as a negative electrode in asymmetric supercapacitors.[87] An asymmetric supercapacitor with a V_2NT_x MXene negative electrode and Mn_3O_4 nanowalls as a positive electrode exhibited a cell voltage of 1.8 V in an aqueous KOH electrolyte. Rafieerad *et al.* reported a novel $Ta_4C_3T_x$ MXene–tantalum oxide (TTO) hybrid as a compatible material for supercapacitor electrodes.[137] With a 20% higher surface area than oxidized $Ta_4C_3T_x$, the hybrid structure exhibited a volumetric capacitance of 447 F cm^{-3} at 1 mV s^{-1}. Mo_2CT_x films obtained from Mo_2Ga_2C exhibited high specific capacitance and good rate capability owing to their defective porous structures.[151] In addition, the conductive carbon backbone and transition metal oxide/hydroxide surface chemistry of Mo_2CT_x MXenes enabled them to be electrochemically active like MoO_3. Persson *et al.* demonstrated that the electrochemical properties of MXenes could be tuned by tailoring their structure.[50] The i-MXene $(Mo_{2/3}Y_{1/3})_2C$ exhibited a 40% higher volumetric capacitance than its $Mo_{1.33}C$ counterpart in the KOH electrolyte. However, a reverse trend was observed with an H_2SO_4 electrolyte, indicating that the influence of vacancies strongly depended on the type of electrolyte. Similarly, the in-plane divacancy ordered 2D $W_{1.33}C$ MXene obtained by etching Al from $(W_{2/3}Sc_{1/3})_2AlC$ and $(W_{2/3}Y_{1/3})_2AlC$ was also demonstrated to be suitable electrode materials for supercapacitors.[77]

The volumetric capacitance of a 3 μm-thick free-standing $Mo_{1.33}C$ electrode was 28% higher than that of a 5 μm-thick $Ti_3C_2T_x$ electrode (Fig. 7f).[52] However, many divacancies in $Mo_{1.33}C$ films led to decreased stability in H_2SO_4 compared to Mo_2C MXene films. Anasori *et al.* reported that the electrochemical properties of DTM MXenes Mo_2TiC_2, $Mo_2Ti_2C_3$, and Cr_2TiC_2 were controlled by the outermost Mo and Cr atoms.[48] The electrochemical properties of the solid solution MXenes could be tuned by altering the ratios of the metals and the surface terminations.[103] For example, $Mo_{2.7}V_{1.3}C_3$ showed an excellent volumetric capacitance of 860 F cm^{-3} compared to other compositions, such as $Mo_2V_2C_3$ (680 F cm^{-3}) and MoV_3C_3 (450 F cm^{-3}).[103] In addition, the type of electrolyte influenced the capacitive behavior and the interlayer spacing of $Mo_{2.7}V_{1.3}C_3$ MXenes. The hydrophilic cations Mg^{2+}, Li^+, and Na^+ from respective 1 M $MgSO_4$, 1 M Li_2SO_4, and 1 M Na_2SO_4 electrolytes resulted in the expansion of interlayer spacing in contrast to K^+ (from the 0.5 M K_2SO_4 electrolyte) which resulted in the contraction of the interlayer spacing. Furthermore, in acidic electrolytes, the $Mo_{2.7}V_{1.3}C_3$ MXenes exhibited faradaic redox behavior, whereas, in non-acidic electrolytes, the MXene exhibited electrical double-layer capacitor-like behavior.

Besides engineering the interlayer spacing of non-Ti MXenes, optimizing their porosity and morphology is highly

important. The synthesis techniques should be optimized to obtain non-Ti MXenes with high conductivity and a large surface area for better storage performance. Furthermore, research must progress in developing non-Ti MXene-based flexible transparent electrodes and in studying the device performance of the non-Ti MXenes in organic electrolytes for industry-level applications.

5.3 Electrocatalysis

With high electronic conductivity, hydrophilicity, thermal stability, rich surface chemistry, and active basal planes, MXenes are used as stable electrocatalysts.[43,152] Besides titanium-based MXenes, various other MXene compositions have been evaluated to be active electrocatalysts for the hydrogen evolution reaction (HER), oxygen evolution reaction (OER), CO_2 reduction reaction (CO_2RR), and nitrogen reduction reaction (NRR).[43,126,152,153] The highly conductive basal plane offering abundant active sites, the ability to be synthesized in varying layers, and the ability to remain stable under negative potentials enable non-Ti MXenes to be potential catalysts for the HER.[142] With smaller Gibbs free energy of adsorption (ΔG_H = 0.048 eV), Mo_2CT_x exhibited better HER activity and stability than Ti_2CT_x (ΔG_H = 0.358 eV).[142] Mo_2CT_x MXene achieved an overpotential of 305 mV at 10 mA cm^{-2} and remained stable with a slight decrease in activity after 30 cycles in contrast to Ti_2CT_x, as shown in Fig. 8a. Furthermore, the per-site activity of Mo_2CT_x determined through the turnover frequency was much higher than that of Ti_2CT_x. The higher-order MXene $V_4C_3T_x$ is highly active and has been reported as an efficient electrocatalyst for the HER, OER, and NRR.[43,99,126] When $V_4C_3T_x$ was tested for HER activity over 100 cycles, loss of oxide species from the surface of MXene was observed.[43] The loss of oxide species did not affect the HER activity. Instead, the overpotential required to reach 10 mA cm^{-2} decreased by 200 mV, demonstrating that the HER activity comes from vanadium atoms in $V_4C_3T_x$ and not from the surface oxide species. The electrocatalytic activity of MXenes could be further improved by forming heterostructures. With a low NRR energy barrier and strong adsorption towards N_2, Ni nanoparticles loaded on $V_4C_3T_x$ exhibited a higher ammonia yield rate (3.41 μg h^{-1} cm^{-2} at 0.2 mA cm^{-2}) and faradaic efficiency (8.04%) than $Ti_3C_2T_x$ and $Ti_3C_2T_x$/FeOOH (Fig. 8b and c).[126]

Using DFT calculations, Cheng *et al.* predicted that Cr_2CO_2 could be used as a bifunctional catalyst for water splitting.[152,154] It was predicted that the concentration of protons in the solvent could alter the HER performance of Cr_2CO_2, and a stable performance could be obtained at high proton concentrations.[154] Zhang *et al.* investigated the effect of surface terminations on the HER activity of Nb_2C MXene.[154] It was deduced that

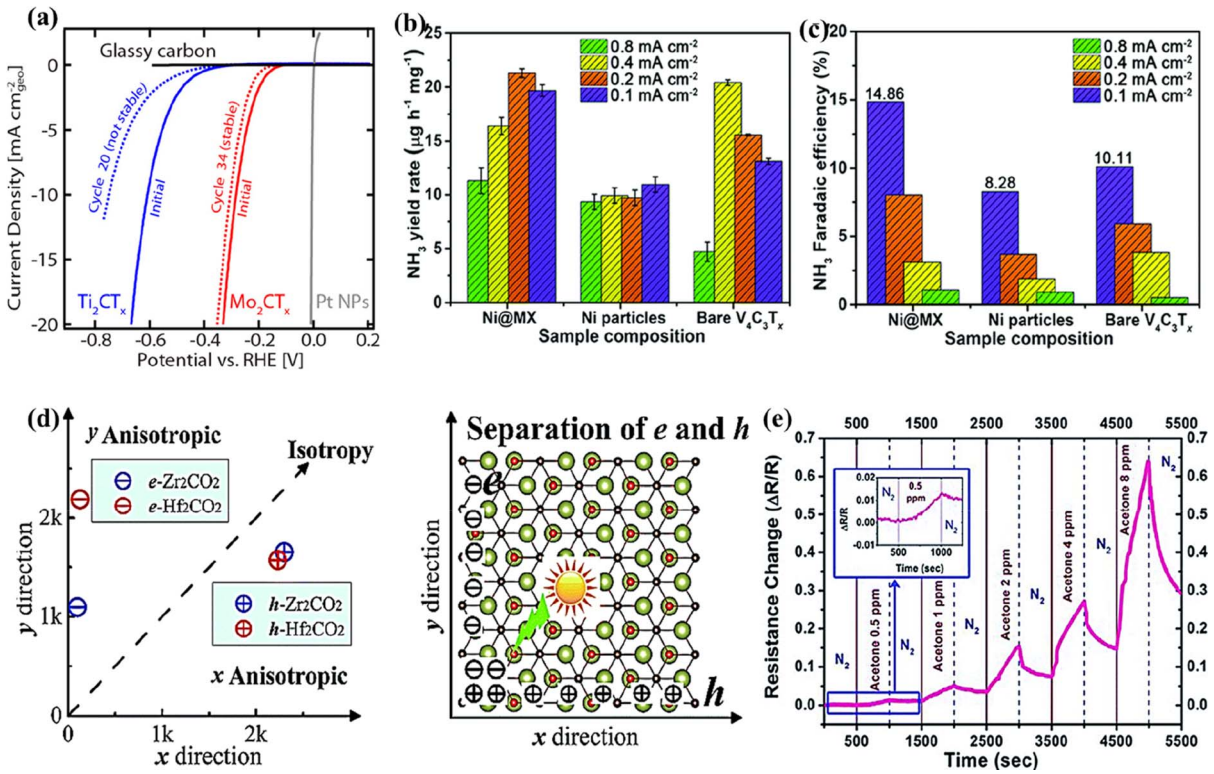

Fig. 8 (a) HER activity comparison of Mo_2CT_x and Ti_2CT_x MXenes. Reproduced with permission from ref. 142 copyright 2016, American Chemical Society. (b) Ammonia yield rate and (c) faradaic efficiency of the Ni@$V_4C_3T_x$ nanocomposite, Ni particles, and $V_4C_3T_x$ MXene. Reproduced with permission from ref. 126 copyright 2021, Royal Society of Chemistry. (d) The carrier mobility of 2D Zr_2CO_2 and Hf_2CO_2 as a function of directions (left) and the schematic picture for the separation of photogenerated electron–hole pairs (right). Reproduced with permission from ref. 156 copyright 2016, Royal Society of Chemistry. (e) The sensor responses of the $V_4C_3T_x$ film to different concentrations of acetone from 0.5 ppm to 8 ppm at room temperature; the inset shows the response to 0.5 ppm acetone from ref. 127.

increased F-terminations on Nb_2C MXene/Pd nanoparticles weaken the hydrogen adsorption, leading to enhanced HER activity compared to their O-terminated counterpart.

Although the electrocatalytic performances of non-Ti MXenes have been reported in the literature, identifying the catalytic pathways and reaction mechanisms remains challenging. Future research must focus on combining the *in situ* characterization techniques with experimental results and theoretical simulations to identify the true catalytic sites as well as the mechanism.

5.4 Other notable applications

Besides the energy-related applications mentioned above, non-Ti MXenes have been employed for various other applications such as photonics, spintronics, electronic sensors, biomedical, environmental remediation, electromagnetic interference shielding (EMI), *etc.*[68,102,114,128,155,156]

Ab initio calculations predicted that Zr_2CO_2 and Hf_2CO_2 MXenes are efficient candidates for photocatalytic water splitting.[156] Their high stability in water, good optical absorption from 300 to 500 nm, and high anisotropic carrier mobility facilitating migration and separation of electron–hole pairs enabled them to be efficient photocatalysts for water splitting (Fig. 8d). Peng *et al.* reported that the type of synthesis method influenced the dye degradation ability of MXenes.[68] The Nb_2C MXene synthesized through the hydrothermal method had a larger surface area than their HF-etched counterparts, enabling the former to adsorb methylene blue faster. The Nb_2C MXene also finds applications as an optical switch in nonlinear photonics due to its change in the nonlinear absorption response in the near-infrared region.[117] The half-metallicity induced by the Cr d electrons and the ferromagnetic to antiferromagnetic transition induced by the surface functional groups impart unique magnetic and electronic properties to Cr_2C MXene.[114] With such tunable properties, the Cr_2C MXenes might find applications in spintronics and electronics. Khazaei *et al.* reported that $M'_2M''C_2O_2$ (M = Mo, W; M = Ti, Zr, Hf) MXenes were topological insulators with large bandgaps due to the strong spin–orbit coupling between the metals M′ and M″.[157] In addition, $M'_2M''_2C_3O_2$ with four transition metal layers were found to be topological semimetals.

Zhao *et al.* reported the fabrication of a resistive-type $V_4C_3T_x$ acetone sensor, which showed high selectivity towards acetone in a mixture of acetone and water vapors.[127] The change in the resistance of the $V_4C_3T_x$ film upon the application of DC voltage was used as the sensing signal. At a very low temperature of 25 °C, the $V_4C_3T_x$ acetone sensor could efficiently detect a low concentration of 1 ppm (Fig. 8e), which was lower than the threshold of diabetes diagnosis (1.8 ppm). Thus, the non-Ti $V_4C_3T_x$ MXene could be used for faster and early diagnosis of diabetes. Similarly, with the ability to detect carcinogenic molecules, a Ta_2C MXene-based sensor was reported to find applications in biochemistry and food safety detection.[155] The i-MXene $W_{1.33}C$ has been reported as an efficient photothermal agent for multimodal imaging and photonic tumor hyperthermia.[128] The $W_{1.33}C$ nanosheets exhibited a photothermal conversion effectiveness of 32.5% in near-infrared (NIR) I and

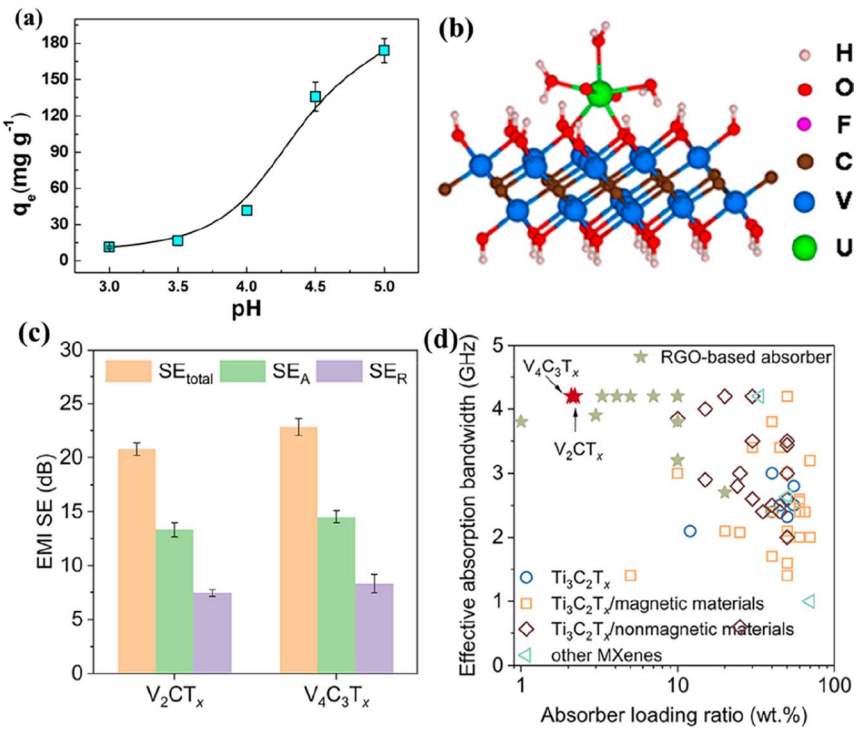

Fig. 9 (a) Adsorption of uranium on V_2CT_x as a function of pH and the adsorption configuration (b). Reproduced with permission from ref. 158 copyright 2016, American Chemical Society. (c) The average EMI shielding effectiveness of V_2CT_x and $V_4C_3T_x$ coatings on glass substrates and (d) EM wave absorption performance of $V_{n+1}C_nT_x$/PU composites compared with reported $Ti_3C_2T_x$-based composites and other materials from ref. 159.

49.3% in NIR II. Furthermore, when the $W_{1.33}C$ nanosheets with a strong NIR absorption band were surface modified with bovine serum albumin (BSA), they exhibited further enhanced photothermal conversion efficiency, rapid degradation, and biocompatibility.

The HF-etched V_2CT_x is reported to efficiently remove actinides from aqueous solutions, making it beneficial for nuclear waste treatment.[158] The V_2CT_x MXene demonstrates the adsorption of uranium with an uptake capacity of 174 mg g^{-1}, as shown in Fig. 9a. DFT calculations revealed that the uranyl ions coordinate with adsorption sites (such as –OH, –O, and –F) on the V atoms of V_2CT_x MXene, forming bidentate adsorption configurations (Fig. 9b). In addition, the $V_{n+1}C_nT_x$ ($n = 1$ or 3) MXenes have also been reported to be effective for EMI shielding.[159] When spray-coated on a glass substrate, V_2CT_x and $V_4C_3T_x$ achieved excellent shielding at thicknesses of 530 nm and 600 nm, respectively. The reflection ratio (>0.8 as shown in Fig. 9c) indicates that the EMI shielding is mainly due to reflection. Furthermore, the $V_{n+1}C_nT_x$–polyurethane (PU) composite effectively absorbs over 90% of EM waves, outperforming $Ti_3C_2T_x$ composites and other materials (Fig. 9d).

6. Theoretically predicted non-Ti MXenes

The continuous expansion of the MAX family to 155 resulted in an increasing number of MXene compositions.[34] About 30 MXenes have been synthesized today, and dozens have been predicted to be feasible. Furthermore, the introduction of o-MAX and i-MAX phases led to the further expansion of the MXene family. The current enormous research efforts focused on Ti MXenes have overlooked the other members of the MXene family. In an attempt to stimulate researchers working on MXenes to realize the theoretically predicted non-Ti MXenes, which are expected to exhibit better performance than Ti MXenes, we briefly discuss their unique properties predicted through theoretical computations. As every MXene experimentally synthesized today was once a predicted MXene, a clear understanding of the predicted properties and the influence of chemistry and structure on their properties would greatly help to synthesize them.

6.1 Predicted monometallic non-Ti MXenes

Theoretically predicted monometallic MXenes such as Hf_2C, Sc_2C, Zr_2C, W_2C, Zr_2N, Zr_3N_2, Hf_2N, Cr_2N, Ni_2N, Mn_2N, MVN (M = Ti, V, and Cr), and Mo_2CN are expected to exhibit intriguing structural, magnetic, electronic, and optical properties.[29,114,160–167] DFT studies are powerful tools that help to predict targeted material design, properties, and characterization without going through long trials and time-consuming experimentation. In order to identify the suitable MAX phase that can lead to the successful synthesis of MXenes, some of the most critical parameters such as formation energy, the number of layers, M atom, Bader charge, system mass, and cohesive energy need to be considered for encoding the strength of the M–X bond, overall thermodynamic stability, and actual charge distribution.[168] In the detailed theoretical analysis on the exfoliation possibility of MAX phases conducted by Khazaei *et al.*, it was predicted that the MAX phases Cr_2GaN, Cr_2GaC, Hf_2InC, Hf_2TlC, Hf_2PbC, Hf_2SnC, Hf_2AlC, Zr_2AlC, and Zr_2InC could be exfoliated to their corresponding MXenes.[169] This prediction was made by examining the electronic structures, force constants, static exfoliation energies, and bond strengths. Their analysis showed that the force constant (strength of bond) for A atoms in MAX was directly proportional to the exfoliation energy and predicted that the MAX phases with large force constants are challenging to be exfoliated to MXenes.

The electronic and magnetic properties of the predicted non-Ti MXenes were reported to be influenced mainly by surface terminations, strain, and pressure.[160,170,171] Using first-principles calculations, it was predicted that O-terminated Hf_2C would transition from metallic to semiconducting with a bandgap of 1 eV.[29] Ougherb *et al.* illustrated that partial substitution of O terminations in semi-conducting Hf_2CO_2 with S led to the formation of Hf_2COS with metallic characteristics.[171] The Bader charge calculation revealed increased impulsive interaction around Hf–S and Hf–O bonds with the substitution of S, which increased the covalency of Hf_2COS. Like H_2C, Sc_2C was also transformed from metallic to semi-conducting upon functionalization with –F, –OH, and –O with respective band gaps of 1.03, 0.45, and 1.8 eV.[29] Similarly, in the case of Janus Sc_2CTT' (T, T′ = H, O, OH, F, Cl), 2D Sc_2COCl had a half-metallic gap of 0.98 eV and a Curie temperature of 292 K, whereas Sc_2COOH had a half-metallic band gap of 0.61 eV and a Curie temperature of 153.8 K.[172]

The ferromagnetic properties of the bare and surface passivated structures of lower-order nitride MXenes based on Fe, Co, and Ni were theoretically determined using DFT.[163] The bare Fe_2N and Co_2N MXenes did not show any ground state configuration, while the passivated $Fe_2N(OH)_2$, Fe_2NO_2, and Co_2NO_2 exhibited ferromagnetic ground states. In the case of Ni_2N, surface passivation with any of the F, OH, and O atoms had no impact on the ferromagnetic ground states displaying half-metallicity (100% spin polarization). The absence of non-trivial imaginary frequencies in the phonon dispersion results of Ni_2NT_2 (T = F, OH, and O) MXene indicated its high stability. Ni_2NO_2 attained the highest Curie temperatures of 3300 K as compared to Ni_2NF_2 (1800 K) and $Ni_2N(OH)_2$ (2400 K), owing to its higher relative energies of the antiferromagnetic configuration and more significant exchange parameters. Using spin-polarized DFT, Cr_2NT_2 (T = O, F, OH) MXenes were investigated as good 2D half-metallic ferromagnetic materials as they satisfied the four criteria of higher structural stability, high Curie temperatures, ferromagnetic ground states, and half-metallic bands.[166] The partial density of states curves showed significant gaps in the minority spin channels in all the functionalized Cr_2NT_2 materials proving their half-metallic character. The negative formation energies of the functional groups indicated their strong interaction with transition metals, and they predicted that it is possible to synthesize Cr_2NT_2 MXene.

The electronic and magnetic properties of the predicted non-Ti MXenes could also be tuned by strain engineering.[170,173] At

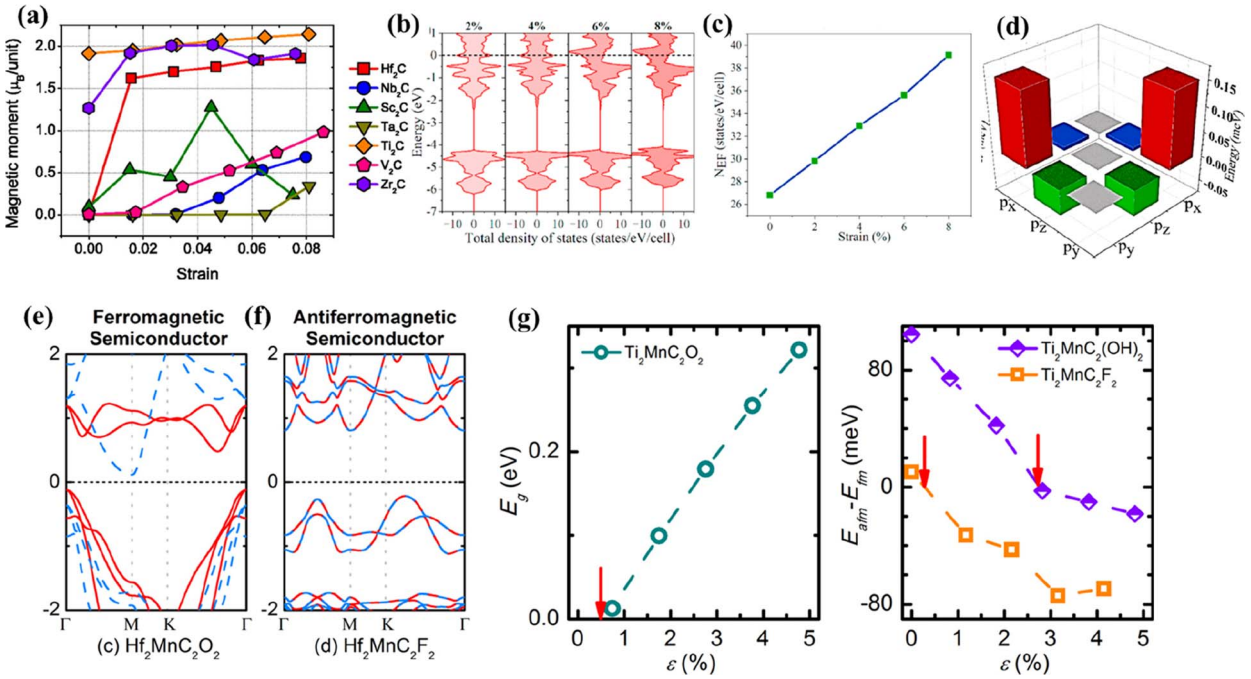

Fig. 10 (a) Dependence of magnetic moments of various MXenes on the applied strain. Reproduced with permission from ref. 173 copyright 2014, AIP Publishing. (b) The densities of states of Zr_2N at tensile strains of 2%, 4%, 6%, and 8%, respectively. Fermi energy is located at zero energy, (c) the number of density of states at the Fermi level (N_{EF}) as a function of biaxial strain in the nonmagnetic state, and (d) the energy difference of spin–orbit coupling matrix elements of the Zr-p orbital. Reproduced with permission from ref. 164 copyright 2021, Elsevier Ltd. (e) Electronic band structure of the ferromagnetic semiconductor $Hf_2MnC_2O_2$, (f) electronic band structure of the antiferromagnetic semiconductor $Hf_2MnC_2F_2$, and (g) effect of tensile in-plane strain (ε) on the band gap (E_g) and magnetic properties of $Ti_2MnC_2T_x$. Reproduced with permission from ref. 180 copyright 2017, American Chemical Society.

the strain-free state, Hf_2C did not display magnetism; however, with 1.8% mechanical strain, the magnetic moment was elevated to be 1.5 μ_B per unit, indicating ferromagnetism (Fig. 10a).[173] This change in magnetic properties was attributed to the band shift of Hf (5d) states. Hf_2C was predicted to bear large elastic strains as the structure was stable with no phase transition. Similarly, Wang *et al.* predicted the nonpolar to polar and metal to semiconductor transition of F-functionalized Hf_2C upon subjecting it to biaxial compressive strain.[170] Lee *et al.* predicted that upon application of 2% strain to monolayer Sc_2CO_2, there would be a transition from indirect to direct bandgap, beneficial for optical devices.[174] With a further increase in the tensile strain from 0 to 5%, the band gap of the system was reduced.

A similar theoretical study published recently by Li *et al.* on the pressure-induced engineering of the bandgap of Sc_2CF_2 also indicated the reduction in the bandgap from 1.023 eV to 0.024 eV for a pressure of 9 GPa, thereby converting Sc_2CF_2 from a semiconductor to a metal.[160] Furthermore, the work function gradually increased under the pressure of 9 GPa from 4.803 to 5.079 eV. The work function of Sc_2CF_2 was smaller than that of $Ti_{n+1}C_nT_x$ (T = O, F). The effect of bi-axial strain on the magnetic properties of Zr_2N MXene was studied by Yue *et al.*[164] They reported that with zero strain, Zr_2N MXene exhibited antiferromagnetic nature at the ground state and was converted to ferromagnetic when the applied strain level reached 4%. This change in nature was attributed to increased densities at the Fermi level with the applied strain (Fig. 10b and c). The magnetic anisotropy energy of Zr_2N decreased with the strain level due to the spin–orbit interactions between the occupied and vacant p_x/p_y states of the Zr atoms (Fig. 10d).

Besides strain and surface terminations, the phase of the MXene is also found to influence its properties.[175,176] The O-terminated 1T W_2C MXene was predicted to be a topological insulator with an indirect bandgap of 0.194 eV.[175] However, the more stable O-functionalized 2H-W_2C MXene exhibited a semiconducting nature with a bandgap of 0.199 eV.[176] 2H-W_2CO_2 had a Young's modulus of 351 N m^{-1}, which is higher than that of graphene. The O-functionalization is predicted to improve the structural stability and thermal conductivity of W_2C MXene. Furthermore, the properties of MXenes could also be altered by varying their geometrical conformations.[129]

Theoretical analysis also predicted that these superb properties could enable the predicted non-Ti MXenes to be effectively used in spintronic, energy storage, and conversion devices.[162,165,177] Non-Ti MXenes were predicted to show magnetic behavior with separated bands near the Fermi level, which is promising for next-generation spintronic devices.[162] The Young's modulus (γ) of the material defines its ability to resist deformation against stress and pressure in the elastic deformation range. Using DFT calculations, Zhang *et al.* predicted that O-terminated Zr_2C MXene with O-groups located

above the opposite metal atoms were energetically more favorable with large cohesive energies.[161] With excellent electrical conductivity, carrier mobilities, low diffusion barrier, good electron–hole separation efficiency, *etc.*, Zr_2CO_2 MXenes are expected to be suitable for energy applications.[129,161] Theoretical calculations revealed that Sc_2C MXene had low diffusion barriers of 0.018 and 0.012 eV for Li and Na ions, respectively.[178] The diffusion barrier of Sc_2C MXene for Li ions was predicted to be much less than that of Ti_3C_2 MXene (0.068 eV), resulting in high mobility and cycling performance. Furthermore, Sc_2C MXene exhibited low average electrode potentials of 0.32 V for Li and 0.24 V for Na, beneficial for low-charging voltage applications. Although $Mo_3C_2T_x$ and Ti_3C_2 are isostructural, the nature of surface Mo atoms in $Mo_3C_2T_x$ significantly differentiates their electrochemical properties.[48] With lower Li adsorption energies than Ti_3C_2, $Mo_3C_2T_x$ MXenes are suitable electrodes for Li-ion batteries.

With the help of DFT calculations, Zhan *et al.* predicted that Zr-based nitride MXenes (Zr_2N, Zr_3N_2, and Zr_4N_3) could possess the best areal capacitance.[165] The authors concluded that the nitride MXenes have better capacitive performance than their carbide counterparts due to the Fermi level shifts that enabled the nitride MXenes to become more metallic and thus increased capacitance. The ferromagnetism and half-metallic transport characteristics of Mn_2NT_x MXenes with different surface terminations (T = O, OH, and F) were explored using crystal field theory.[167] The stability of the magnetic ordering was determined by predicting the Curie temperature through Monte Carlo simulations. Curie temperature in the range of 1877 to 566 K and the significant magnetic moments enabled them to be attractive for 2D spintronic applications. Mn_2NT_x showed robust intrinsic half-metallicity with a wide bandgap for the minority spin for all three surface terminations O, OH, and F.

With low theoretical overpotential, high stability, and selectivity, H-terminated W_2C was proposed as a potential candidate for catalysis.[177] Johnson *et al.* performed a theoretical screening on 65 bare and functionalized M_2XT_x MXenes (M = Ti, V, Zr, Nb, Mo, Ta, W; X = C, N; T_x = bare, H, O, or N) to identify the suitable MXene species for an efficient NRR.[177] Selectivity analysis and Pourbaix stability diagrams revealed that bare MXenes are unstable under NRR conditions, and H-terminated W_2CH_2 was the only MXene predicted to be highly stable with low theoretical overpotential and high selectivity towards the NRR. By analyzing the conversion pathway for carbon dioxide to methane through DFT calculations, Xiao and Zhang predicted that Ta_3C_2 and Sc_3C_2 MXenes are efficient catalysts for the CO_2RR.[153]

There are only a couple of theoretical studies reported on non-Ti carbonitride MXenes. Wei *et al.* determined the thermodynamic stability and electrocatalytic properties of $Mo_2(C_xN_{1-x})T_2$ (T = F, OH, and O) MXene.[179] The co-existence of carbon and nitrogen in molybdenum-based carbonitride MXene $Mo_2(C_xN_{1-x})T_2$ (T = F, OH, and O) was predicted to reduce the interaction between surface O atoms and H* leading to excellent HER activity and stability. Furthermore, the presence of 0.5 O* and 0.5 OH* monolayers on $Mo_2(CN)T_2$ increased its thermodynamic stability, with the oxygen atoms serving as active catalytic sites for the HER.

6.2 Predicted DTM MXenes

Although very few DTM MXenes show experimental evidence, the possibility of synthesizing many DTM MXenes, including ordered and solid solutions, was predicted through theoretical computations.[157,180,181] The phase stability of ordered and disordered 312 and 413 MAX phases was investigated through first-principles calculations by Dahlqvist and Rosen.[182,183] They predicted that at 0 K, stable and ordered MAX phases could likely be obtained when the order–disorder temperature ($T_{disorder}$) was greater than 1773 K.[182] For $T_{disorder}$ < 1773 K, MAX phases were likely to be obtained as disordered structures. Furthermore, they predicted that unstable MAX phases at 0 K could be stabilized at higher temperatures resulting in disordered solid solutions. In their recent work, using predictive phase stability calculations, they showed that the formation of ordered and disordered MAX phases depended on the size of the metals M′ and M″ and the difference in electronegativity between M′ and A.[183] Using high-throughput computations, Tan *et al.* showed that the degree and type of ordering depended on the composition and temperature of the alloying system.[184] Monte Carlo simulations revealed that when Mo-rich MXenes were alloyed with M = Ti, V, Nb, and Ta, the resulting MXenes $(M_{1-x}Mo_x)_3C_2$ had their surface layers occupied with Mo. Furthermore, the ordering of the metal layers was expected to be present at high temperatures. However, Nb and V elements were intermixed well to form solid solutions $(Nb_{1-x}V_x)_3C_2$.

Khazaei *et al.* predicted that $M'_2M''C_2O_2$ (M′ = Mo, W; M″ = Ti, Zr, Hf) were topological insulators with a maximum bandgap of 0.285 eV within the generalized gradient approximation.[157] However, the electronic structures of the thicker MXenes $M'_2M''_2C_3O_2$ (M′ = Mo, W; M″ = Ti, Zr, Hf) revealed that they were nontrivial topological semimetals. Of these predicted MXenes, $Mo_2TiC_2T_x$ and $Mo_2Ti_2C_3T_x$ (T_x = F, O, and OH) have been synthesized. Despite the lack of experimental evidence for ordered DTM MXenes with M′ = Ti, many theoretical predictions exist on the potential use of Ti as M′ metal.[180,185] For example, Dong *et al.* predicted the magnetic and electronic properties of $Ti_2MnC_2T_x$ (T = F, O, and OH) ordered DTM MXenes.[180] Using DFT, they confirmed that the $Ti_2MnC_2T_x$ MXene is ferromagnetic with semimetallic/metallic ground states regardless of surface terminations. Similar to monometallic MXenes, the properties of the predicted DTM MXenes could also be changed by the type of the transition metal, surface terminations, or introducing strain. Replacing Ti with Hf in $Ti_2MnC_2O_2$ and $Ti_2MnC_2F_2$ resulted in ferromagnetic or antiferromagnetic semi-conducting ground states (Fig. 10e and f). The $Ti_2MnC_2O_2$ MXene could change from a ferromagnetic semimetal to a ferromagnetic semiconductor under a tensile strain of $\varepsilon > 0.5\%$. In addition, $Ti_2MnC_2(OH)_2$ and $Ti_2MnC_2F_2$ could change to antiferromagnetic under the strains $\varepsilon = 2.8\%$ and $\varepsilon = 0.3\%$, respectively (Fig. 10g).

Similarly, Yang *et al.* reported the change in the magnetic and electronic properties of $Cr_2M_2C_3T_2$ (M = Ti, V, Nb, and Ta; T

= OH, O, and F) under the influence of strain.[186] Theoretical calculations showed that the Cr-3d orbital, the main origin of the magnetic moment, was more localized with the increase in strain. At the same time, the decrease in the density of states near the Fermi level indicated the reduction in conductivity with the introduction of strain. It was predicted that O-terminated $Hf_2MnC_2T_x$ and $Hf_2VC_2T_x$ MXenes are ferromagnetic semiconductors, while their OH or F-terminated counterparts are antiferromagnetic.[180] The magnetic tunnel junction based on $ScCr_2C_2$ was predicted to exhibit a tunnel magnetoresistance ratio of 176 000%, and $ZrCr_2C_2(OH)_2$ was predicted to possess a Néel temperature of 425 K.[187] The bandgap and magnetism in DTM MXenes were predicted by Sun *et al.*[188] Based on the surface metal and the terminations, they predicted that the Cr–N and Mn–N series could transition from a metal to an insulator. They also predicted that bare $TiMn_2N_2$ was metallic, while its F- terminated counterpart had a wide band gap of 1 eV.

The bare Mo-based DTM MXene Mo_2MC_2 (M = Sc, Ti, V, Zr, Nb, Hf, Ta) was predicted to exhibit superior electrochemical properties.[181] The thermodynamic stability and catalytic performance of $M'_2M''C_2T_x$ and $M'_2M''_2C_3T_x$ (M′ = Cr, V, Ti, or Nb; M″ = Nb, Ta, Ti, or V; and T = O and/or OH) ordered DTM MXenes were predicted using DFT computations.[185] Crystal orbital Hamilton population analyses, Bader charge, and density of states revealed that the hydrogen binding strength on the functionalized DTM MXene depended on the M′–O bond. The weaker the M′–O, the stronger the bonding between the adsorbed H and O*. Out of the 24 DTM MXenes screened for HER activity, 18 MXenes had theoretical overpotentials smaller than 0.2 V, with $Mo_2NbC_2O_2$ exhibiting the lowest overpotential. Furthermore, the HER performance of $Ti_3C_2O_2$ ($\Delta G_H = 0.01$ eV) was predicted to be modified by adding an inner metal layer such as Ta to form $Ti_2TaC_2O_2$ ($\Delta G_H = 0.008$ eV) DTM MXene. It was determined that the outermost metal species, which dominate the basal plane chemistry, play a vital role in the catalytic activity of ordered DTM MXenes.

Among the O-terminated DTM carbonitrides $M'_2M''CNO_2$ (M′ = Ti, V, Cr, Zr, Nb, Mo, Hf, Ta; M″ = Ti, V, Cr, Zr, Nb, Mo, Hf, Ta), Ti_2NbCNO_2, Mo_2TiCNO_2, and Ti_2VCNO_2 were predicted to be thermodynamically stable and might be potentially synthesized.[189] Among the different combinations of the tested MXenes for HER activity, Ti_2NbCNO_2 and Ti_2ZrCNO_2 showed the maximum HER performance with a small ΔG_H of 0.02 eV.

In general, the MAX phases with low bond strengths and exfoliation energies could be easily exfoliated to 2D MXenes. Developing new etching and processing strategies is crucial to exfoliate the MAX phases successfully. Furthermore, theoretical studies should consider accurate experimental conditions for better prediction. Most of the simulations consider a defect-free crystal with pristine or heterogeneous terminations. However, these considerations of ideal MXenes are not practical. Thus, heterogeneous terminations and defects in the crystal structures should be considered to match the actual experimental observations. Besides the optimized etching conditions, much effort has to be put on optimizing the bottom-up synthesis techniques like CVD to realize the theoretically predicted MXenes.

7. Summary and outlook

The continuous developments in synthetic protocols and new etching methods have accredited MXenes as the fastest-growing family of 2D materials. Despite the fact that the MXene family has expanded with the successful synthesis of many monometallic MXenes, higher order solid solution MXenes such as $M_5C_4T_x$, o-MXenes, and i-MXenes, most of the MXene papers published even now are based on Ti-based MXenes. Although the Ti-based MXenes have shown great potential for many applications, the remarkable structural, mechanical, magnetic, and electronic properties of non-Ti MXenes stress the need to pay equal attention to them to unleash their full potential. As detailed investigations on the non-Ti MXenes will uncover their exciting and untold features compared to Ti-based MXenes, this review provides a comprehensive overview of their synthetic methods, unique properties, and applications. Since myriad compositions of non-Ti MXenes are theoretically predicted and are expected to exhibit better performance than Ti-based MXenes, their predicted unique properties are discussed to stimulate researchers to focus on synthesizing them. The current challenges and the future research directions to delve into non-Ti MXenes are briefly depicted in Fig. 11 and detailed as follows:

7.1 Limited synthesis routes

Most of the carbide-based non-Ti MXenes reported are obtained through HF etching. Besides toxicity, HF leads to F-terminated MXenes unsuitable for biomedical applications. Although there are theoretical predictions on the conversion of F-terminations to O with the progress of the reaction, experimental evidence is needed to verify this.[154] Furthermore, the acid–salt and molten salt etching produce *in situ* HF. Although alternative etching methods such as hydrothermal, electrochemical, and Lewis

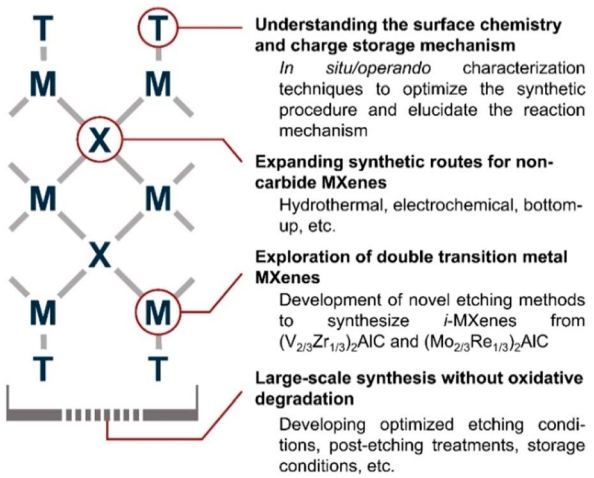

Fig. 11 Summary of challenges and future research directions of non-Ti MXenes.

acid are implemented to synthesize less toxic non-Ti MXenes, they are not widely explored.[79] Moreover, the bottom-up approaches to synthesizing MXenes should be well investigated to realize the theoretically predicted MXenes and the mass production of MXenes. Most of the MAX phases synthesized have Al as the A element, albeit the availability of a wide range of suitable A elements. Thus researchers must probe into synthesizing MAX phases with A elements other than Al. In addition, layered ternary solids could be used as precursors to realize the predicted MXenes whose MAX phase formation is considered tedious. Besides the urgency to synthesize the theoretically predicted non-Ti MXenes, most of the synthesized MXenes, such as $Zr_3C_2T_x$, $Hf_2C_2T_x$, V_2NT_x, *etc.*, need much detailed analysis of their properties and applications.

7.2 Limited analysis on DTM MXenes

It is also important to note that although i-MXenes were first reported in 2017, their progress has not been remarkable and most of the studies reported on them are from the same research group. Novel etching methods or conditions should be designed to synthesize i-MXene from the i-MAX phase $(V_{2/3}Zr_{1/3})_2AlC$ synthesized in 2017 and rare-earth (RE) containing i-MAX phase $(Mo_{2/3}RE_{1/3})_2AlC$ synthesized in 2019.[190,191] The possible reasons for the lack of synthesis reports on the ordered DTM MXenes with $M' = Ti$ must be deliberated. In the case of solid solution MXenes, there are very limited experimental and theoretical studies, although thousands have been predicted. Further research is required to determine the atomic positions and space group of Mo_4VC_4, the higher-order solid solution MXene.[60]

7.3 Fewer reports on nitride MXenes

The fact that there are no experimental reports and only a few theoretical predictions on non-Ti carbonitride MXenes is perplexing. Therefore, more research must be concentrated on synthesizing and exploring the properties and potential applications of non-carbide non-Ti MXenes. In addition, research efforts must also be made to synthesize DTM MXenes from the synthesized DTM MAX phases and to synthesize nitride and carbonitride MXenes.

7.4 Lack of understanding of surface chemistry

As surface terminations influence the properties of non-Ti MXenes, a detailed understanding of the surface chemistry of MXenes is necessary. Griffith *et al.* demonstrated that XRD alone is insufficient for the complete characterization of MAX and MXenes and stressed the importance of nuclear magnetic resonance (NMR) spectroscopy to assess their interfacial chemistry, phase purity, and electronic properties.[192] This work suggested that various other characterization techniques should be coupled with the existing conventional techniques for precise analysis of the MXene properties. *In situ*/*operando* XRD, Raman spectroscopy, TEM, XPS, *etc.*, are essential to optimize the synthesis procedure, elucidate the reaction mechanism and understand the unique properties of MXenes. With the overwhelming theoretical studies, obtaining the experimental proof for predicted non-Ti MXenes and analyzing their properties and potential applications are very compelling at the moment. With the rapid advances in the *in situ*/*operando* characterization techniques, one can foresee that the experimental validation of the theoretical prediction is imminent.

7.5 Difficulty in large-scale synthesis and preventing oxidative degradation

These are the two critical drawbacks of MXenes that have left researchers to ponder the commercialization of MXene. The successful demonstration of the scalable synthesis of $Ti_3C_2T_x$ MXene by Shuck *et al.* is considered equally valid for non-Ti MXenes with similar etching procedures, thus providing a profitable venue for further research.[193] Oxidative degradation is an inherent issue encountered by MXenes due to the harsh etching conditions leading to loss of functional properties. The defects formed on the edges or at the surface during the chemical etching act as active sites for the degradation of MXenes when exposed to water and/or oxygen. This oxidative degradation in MXenes is often explained by using the representative $Ti_3C_2T_x$ MXene.[194] The Ti atoms in the MXene layers are oxidized to form Ti_2O, and C atoms agglomerate to form an amorphous carbon structure. A similar degradation is also expected in non-Ti MXenes as they have identical structures and are usually synthesized under the same conditions. However, with a smaller lateral flake size and the same monolayer thickness as Ti_2C, Nb_2C MXene degrades slower in water.[44] This slow degradation of Nb_2C compared to Ti_2C implies that the material composition and the type of bonding in the monolayer greatly influence the oxidative degradation of MXenes, thus stressing the need to study non-Ti MXenes. Research must also progress in identifying the oxidative degradation of nitrogen-containing MXenes, as none has been reported yet. The oxidative degradation in non-Ti MXenes could be tackled by carefully controlling the purity of parent MAX phases, etching conditions, post-etching treatments, defect passivation, surface layer doping, or forming composites. Furthermore, the storage environment is vital to delaying the oxidative degradation of aqueous dispersions of MXenes. Storing MXenes at low temperatures and under an inert atmosphere (Ar-filled vials) significantly improves their oxidation stability.

Although MXenes were discovered in 2011 and comprise numerous compositions, 83% of the studies are confined to Ti-based MXenes. By varying the transition metal, carbon/nitrogen, functional group, and surface defects, the electrochemical properties of non-Ti MXenes can be effectively tuned, offering great potential for energy conversion and storage applications. Furthermore, non-Ti MXenes have demonstrated significant effectiveness in EMI shielding, wastewater treatment, biomedical, spintronic, and photonic applications. By addressing the challenges stated above, non-Ti MXenes are sure to find applications in many fields beyond what has been covered in this review. We hope that this review will stimulate researchers working on MXenes to explore the myriad compositions of MXenes apart from the conventional Ti-containing MXenes.

Conflicts of interest

The authors declare no conflict of interest.

Acknowledgements

This work was supported by the National Research Foundation of Korea, Grant No. NRF-2020K1A3A1A19088726, NRF-2019R1A6A1A11044070, NRF-2021M3H4A1A02049916, and Department of Science and Technology (DST) under the joint India-Korea bilateral project (INT/Korea/P-52). This work was also supported by the Korea Institute of Energy Technology Evaluation and Planning (KETEP) grant funded by the Korea government (MOTIE), Grant No. 20203020030010, and by the Central Power Research Institute (CPRI), Bangalore (RSOP/21-26/GD/6) and Pandit Deendayal Energy University (PDEU) under the Start-up grant ORSP/R&D/PDPU/2021/NC00/R0069.

References

1 K. S. Novoselov, A. K. Geim, S. V. Morozov, D. Jiang, Y. Zhang, S. V. Dubonos, I. V. Grigorieva and A. A. Firsov, *Science*, 2004, **306**, 666–669.
2 Q. H. Wang, K. Kalantar-Zadeh, A. Kis, J. N. Coleman and M. S. Strano, *Nat. Nanotechnol.*, 2012, **7**, 699–712.
3 C. R. Dean, A. F. Young, I. Meric, C. Lee, L. Wang, S. Sorgenfrei, K. Watanabe, T. Taniguchi, P. Kim, K. L. Shepard and J. Hone, *Nat. Nanotechnol.*, 2010, **5**, 722–726.
4 K. Kalantar-zadeh, J. Z. Ou, T. Daeneke, A. Mitchell, T. Sasaki and M. S. Fuhrer, *Appl. Mater. Today*, 2016, **5**, 73–89.
5 A. Castellanos-Gomez, *J. Phys. Chem. Lett.*, 2015, **6**, 4280–4291.
6 P. Vogt, P. De Padova, C. Quaresima, J. Avila, E. Frantzeskakis, M. C. Asensio, A. Resta, B. Ealet and G. Le Lay, *Phys. Rev. Lett.*, 2012, **108**, 155501.
7 S. Zhang, Z. Yan, Y. Li, Z. Chen and H. Zeng, *Angew. Chem., Int. Ed.*, 2015, **54**, 3112–3115.
8 E. Bianco, S. Butler, S. Jiang, O. D. Restrepo, W. Windl and J. E. Goldberger, *ACS Nano*, 2013, **7**, 4414–4421.
9 P. Vishnoi, M. Mazumder, S. K. Pati and C. N. R. Rao, *New J. Chem.*, 2018, **42**, 14091–14095.
10 Y. Gogotsi and B. Anasori, *ACS Nano*, 2019, **13**, 8491–8494.
11 M. Tahir, A. Ali Khan, S. Tasleem, R. Mansoor and W. K. Fan, *Energy Fuels*, 2021, **35**, 10374–10404.
12 W.-X. Huang, Z.-P. Li, D.-D. Li, Z.-H. Hu, C. Wu, K.-L. Lv and Q. Li, *Rare Met.*, 2022, **41**, 3268–3300.
13 X. Chen, Z. Shi, Y. Tian, P. Lin, D. Wu, X. Li, B. Dong, W. Xu and X. Fang, *Mater. Horiz.*, 2021, **8**, 2929–2963.
14 P. Huang, S. Zhang, H. Ying, W. Yang, J. Wang, R. Guo and W. Han, *Nano Res.*, 2021, **14**, 1218–1227.
15 P. Huang, H. Ying, S. Zhang, Z. Zhang and W.-Q. Han, *J. Mater. Chem. A*, 2022, **10**, 22135–22144.
16 S. Zhang, H. Ying, P. Huang, J. Wang, Z. Zhang, T. Yang and W.-Q. Han, *ACS Nano*, 2020, **14**, 17665–17674.
17 P. Huang, H. Ying, S. Zhang, Z. Zhang and W.-Q. Han, *Adv. Energy Mater.*, 2022, **12**, 2202052.
18 K. L. Firestein, J. E. von Treifeldt, D. G. Kvashnin, J. F. S. Fernando, C. Zhang, A. G. Kvashnin, E. V. Podryabinkin, A. V. Shapeev, D. P. Siriwardena, P. B. Sorokin and D. Golberg, *Nano Lett.*, 2020, **20**, 5900–5908.
19 Z. Li, L. Wang, D. Sun, Y. Zhang, B. Liu, Q. Hu and A. Zhou, *Mater. Sci. Eng., B*, 2015, **191**, 33–40.
20 G. Li, K. Jiang, S. Zaman, J. Xuan, Z. Wang and F. Geng, *Inorg. Chem.*, 2019, **58**, 9397–9403.
21 T. S. Mathis, K. Maleski, A. Goad, A. Sarycheva, M. Anayee, A. C. Foucher, K. Hantanasirisakul, C. E. Shuck, E. A. Stach and Y. Gogotsi, *ACS Nano*, 2021, **15**, 6420–6429.
22 C. Dai, H. Lin, G. Xu, Z. Liu, R. Wu and Y. Chen, *Chem. Mater.*, 2017, **29**, 8637–8652.
23 J. Ran, G. Gao, F.-T. Li, T.-Y. Ma, A. Du and S.-Z. Qiao, *Nat. Commun.*, 2017, **8**, 13907.
24 S. Venkateshalu and A. N. Grace, *Electrochim. Acta*, 2020, **341**, 136035.
25 P. Huang, H. Ying, S. Zhang, Z. Zhang and W.-Q. Han, *Chem. Eng. J.*, 2022, **429**, 132396.
26 X. Fan, Y. Ding, Y. Liu, J. Liang and Y. Chen, *ACS Nano*, 2019, **13**, 8124–8134.
27 S. Hong, G. Zou, H. Kim, D. Huang, P. Wang and H. N. Alshareef, *ACS Nano*, 2020, **14**, 9042–9049.
28 J. Zhou, X. Zha, F. Y. Chen, Q. Ye, P. Eklund, S. Du and Q. Huang, *Angew. Chem., Int. Ed.*, 2016, **55**, 5008–5013.
29 M. Khazaei, M. Arai, T. Sasaki, C.-Y. Chung, N. S. Venkataramanan, M. Estili, Y. Sakka and Y. Kawazoe, *Adv. Funct. Mater.*, 2013, **23**, 2185–2192.
30 L. Li, *Comput. Mater. Sci.*, 2016, **124**, 8–14.
31 M. Naguib, J. Halim, J. Lu, K. M. Cook, L. Hultman, Y. Gogotsi and M. W. Barsoum, *J. Am. Chem. Soc.*, 2013, **135**, 15966–15969.
32 M. Naguib, M. Kurtoglu, V. Presser, J. Lu, J. Niu, M. Heon, L. Hultman, Y. Gogotsi and M. W. Barsoum, *Adv. Mater.*, 2011, **23**, 4248–4253.
33 M. Naguib, O. Mashtalir, J. Carle, V. Presser, J. Lu, L. Hultman, Y. Gogotsi and M. W. Barsoum, *ACS Nano*, 2012, **6**, 1322–1331.
34 M. Sokol, V. Natu, S. Kota and M. W. Barsoum, *Trends Chem.*, 2019, **1**, 210–223.
35 S. Venkateshalu, M. Shariq, N. K. Chaudhari, K. Lee and A. N. Grace, *J. Mater. Chem. A*, 2022, **10**, 20174–20189.
36 K. Liang, A. Tabassum, A. Majed, C. Dun, F. Yang, J. Guo, K. Prenger, J. J. Urban and M. Naguib, *InfoMat*, 2021, **3**, 1422–1430.
37 I. R. Shein and A. L. Ivanovskii, *Comput. Mater. Sci.*, 2012, **65**, 104–114.
38 S. Zada, H. Lu, F. Yang, Y. Zhang, Y. Cheng, S. Tang, W. Wei, Y. Qiao, P. Fu, H. Dong and X. Zhang, *ACS Appl. Bio Mater.*, 2021, **4**, 4215–4223.
39 Z. Wu, C. Li, Z. Li, K. Feng, M. Cai, D. Zhang, S. Wang, M. Chu, C. Zhang, J. Shen, Z. Huang, Y. Xiao, G. A. Ozin, X. Zhang and L. He, *ACS Nano*, 2021, **15**, 5696–5705.

40 J. Mei, G. A. Ayoko, C. Hu, J. M. Bell and Z. Sun, *Sustainable Mater. Technol.*, 2020, **25**, e00156.
41 A. Jastrzebska, A. Szuplewska, A. Rozmysłowska-Wojciechowska, J. Mitrzak, T. Wojciechowski, M. Chudy, D. Moszczyńska, A. Wójcik, K. Prenger and M. Naguib, *ACS Sustainable Chem. Eng.*, 2020, **8**, 7942–7951.
42 J. Zhou, X. Zha, X. Zhou, F. Chen, G. Gao, S. Wang, C. Shen, T. Chen, C. Zhi, P. Eklund, S. Du, J. Xue, W. Shi, Z. Chai and Q. Huang, *ACS Nano*, 2017, **11**, 3841–3850.
43 M. H. Tran, T. Schäfer, A. Shahraei, M. Dürrschnabel, L. Molina-Luna, U. I. Kramm and C. S. Birkel, *ACS Appl. Energy Mater.*, 2018, **1**, 3908–3914.
44 S. Huang and V. N. Mochalin, *ACS Nano*, 2020, **14**, 10251–10257.
45 Z. Liu, L. Zheng, L. Sun, Y. Qian, J. Wang and M. Li, *J. Am. Ceram. Soc.*, 2014, **97**, 67–69.
46 A. VahidMohammadi, J. Rosen and Y. Gogotsi, *Science*, 2021, **372**, eabf1581.
47 W. Hong, B. C. Wyatt, S. K. Nemani and B. Anasori, *MRS Bull.*, 2020, **45**, 850–861.
48 B. Anasori, Y. Xie, M. Beidaghi, J. Lu, B. C. Hosler, L. Hultman, P. R. C. Kent, Y. Gogotsi and M. W. Barsoum, *ACS Nano*, 2015, **9**, 9507–9516.
49 S. Venkateshalu, G. M. Tomboc, B. Kim, J. Li and K. Lee, *ChemNanoMat*, 2022, e202200320, DOI: **10.1002/cnma.202200320**.
50 I. Persson, A. el Ghazaly, Q. Tao, J. Halim, S. Kota, V. Darakchieva, J. Palisaitis, M. W. Barsoum, J. Rosen and P. O. Å. Persson, *Small*, 2018, **14**, 1703676.
51 R. Meshkian, Q. Tao, M. Dahlqvist, J. Lu, L. Hultman and J. Rosen, *Acta Mater.*, 2017, **125**, 476–480.
52 Q. Tao, M. Dahlqvist, J. Lu, S. Kota, R. Meshkian, J. Halim, J. Palisaitis, L. Hultman, M. W. Barsoum, P. O. Å. Persson and J. Rosen, *Nat. Commun.*, 2017, **8**, 14949.
53 J. Halim, J. Palisaitis, J. Lu, J. Thörnberg, E. J. Moon, M. Precner, P. Eklund, P. O. Å. Persson, M. W. Barsoum and J. Rosen, *ACS Appl. Nano Mater.*, 2018, **1**, 2455–2460.
54 Z. Liu, E. Wu, J. Wang, Y. Qian, H. Xiang, X. Li, Q. Jin, G. Sun, X. Chen, J. Wang and M. Li, *Acta Mater.*, 2014, **73**, 186–193.
55 B. Anasori, J. Halim, J. Lu, C. A. Voigt, L. Hultman and M. W. Barsoum, *Scr. Mater.*, 2015, **101**, 5–7.
56 B. Anasori, M. Dahlqvist, J. Halim, E. J. Moon, J. Lu, B. C. Hosler, E. a. N. Caspi, S. J. May, L. Hultman, P. Eklund, J. Rosén and M. W. Barsoum, *J. Appl. Phys.*, 2015, **118**, 094304.
57 B. Anasori, C. Shi, E. J. Moon, Y. Xie, C. A. Voigt, P. R. C. Kent, S. J. May, S. J. L. Billinge, M. W. Barsoum and Y. Gogotsi, *Nanoscale Horiz.*, 2016, **1**, 227–234.
58 Z. Shen, Z. Wang, M. Zhang, M. Gao, J. Hu, F. Du, Y. Liu and H. Pan, *Materialia*, 2018, **1**, 114–120.
59 J. Yang, M. Naguib, M. Ghidiu, L.-M. Pan, J. Gu, J. Nanda, J. Halim, Y. Gogotsi and M. W. Barsoum, *J. Am. Ceram. Soc.*, 2016, **99**, 660–666.
60 G. Deysher, C. E. Shuck, K. Hantanasirisakul, N. C. Frey, A. C. Foucher, K. Maleski, A. Sarycheva, V. B. Shenoy, E. A. Stach, B. Anasori and Y. Gogotsi, *ACS Nano*, 2020, **14**, 204–217.
61 J. Zhou, S. Gao, Z. Guo and Z. Sun, *Ceram. Int.*, 2017, **43**, 11450–11454.
62 M. Han, K. Maleski, C. E. Shuck, Y. Yang, J. T. Glazar, A. C. Foucher, K. Hantanasirisakul, A. Sarycheva, N. C. Frey, S. J. May, V. B. Shenoy, E. A. Stach and Y. Gogotsi, *J. Am. Chem. Soc.*, 2020, **142**, 19110–19118.
63 R. Syamsai, J. R. Rodriguez, V. G. Pol, Q. Van Le, K. M. Batoo, S. F. Adil, S. Pandiaraj, M. R. Muthumareeswaran, E. H. Raslan and A. N. Grace, *Sci. Rep.*, 2021, **11**, 688.
64 E. a. N. Caspi, P. Chartier, F. Porcher, F. Damay and T. Cabioc'h, *Mater. Res. Lett.*, 2015, **3**, 100–106.
65 B. Tunca, T. Lapauw, O. M. Karakulina, M. Batuk, T. Cabioc'h, J. Hadermann, R. Delville, K. Lambrinou and J. Vleugels, *Inorg. Chem.*, 2017, **56**, 3489–3498.
66 Y. Long, Y. Tao, T. Shang, H. Yang, Z. Sun, W. Chen and Q.-H. Yang, *Adv. Sci.*, 2022, **9**, 2200296.
67 K. L. Firestein, J. F. S. Fernando, C. Zhang, C.-E. M. Lewis and D. V. Golberg, *ACS Appl. Nano Mater.*, 2022, **5**, 12117–12125.
68 C. Peng, P. Wei, X. Chen, Y. Zhang, F. Zhu, Y. Cao, H. Wang, H. Yu and F. Peng, *Ceram. Int.*, 2018, **44**, 18886–18893.
69 V. Kamysbayev, A. S. Filatov, H. Hu, X. Rui, F. Lagunas, D. Wang, R. F. Klie and D. V. Talapin, *Science*, 2020, **369**, 979–983.
70 S.-Y. Pang, Y.-T. Wong, S. Yuan, Y. Liu, M.-K. Tsang, Z. Yang, H. Huang, W.-T. Wong and J. Hao, *J. Am. Chem. Soc.*, 2019, **141**, 9610–9616.
71 C. Xu, L. Wang, Z. Liu, L. Chen, J. Guo, N. Kang, X.-L. Ma, H.-M. Cheng and W. Ren, *Nat. Mater.*, 2015, **14**, 1135–1141.
72 E. Ghasali, Y. Orooji, A. Azarniya, M. Alizadeh, M. Kazemzad and TouradjEbadzadeh, *Appl. Surf. Sci.*, 2021, **542**, 148538.
73 R. Meshkian, L.-Å. Näslund, J. Halim, J. Lu, M. W. Barsoum and J. Rosen, *Scr. Mater.*, 2015, **108**, 147–150.
74 Y. Peng, C. Lin, L. Long, T. Masaki, M. Tang, L. Yang, J. Liu, Z. Huang, Z. Li, X. Luo, J. R. Lombardi and Y. Yang, *Nano-Micro Lett.*, 2021, **13**, 52.
75 M. Ghidiu, M. Naguib, C. Shi, O. Mashtalir, L. M. Pan, B. Zhang, J. Yang, Y. Gogotsi, S. J. L. Billinge and M. W. Barsoum, *Chem. Commun.*, 2014, **50**, 9517–9520.
76 R. Meshkian, M. Dahlqvist, J. Lu, B. Wickman, J. Halim, J. Thörnberg, Q. Tao, S. Li, S. Intikhab, J. Snyder, M. W. Barsoum, M. Yildizhan, J. Palisaitis, L. Hultman, P. O. Å. Persson and J. Rosen, *Adv. Mater.*, 2018, **30**, 1706409.
77 R. Meshkian, H. Lind, J. Halim, A. El Ghazaly, J. Thörnberg, Q. Tao, M. Dahlqvist, J. Palisaitis, P. O. Å. Persson and J. Rosen, *ACS Appl. Nano Mater.*, 2019, **2**, 6209–6219.
78 Y. Zhou, F. Meng and J. Zhang, *J. Am. Ceram. Soc.*, 2008, **91**, 1357–1360.
79 S. Venkateshalu and A. N. Grace, in *Fundamental Aspects and Perspectives of MXenes*, ed. M. Khalid, A. N. Grace, A. Arulraj and A. Numan, Springer International Publishing, Cham, 2022, pp. 17–36, DOI: **10.1007/978-3-031-05006-0_2**.

80 Y. Jiang, M. Tian, H. Wang, C. Wei, Z. Sun, M. H. Rummeli, P. Strasser, J. Sun and R. Yang, *ACS Nano*, 2021, **15**, 19640–19650.
81 S. Yazdanparast, S. Soltanmohammad, A. Fash-White, G. J. Tucker and G. L. Brennecka, *ACS Appl. Mater. Interfaces*, 2020, **12**, 20129–20137.
82 Y. Wang, W. Zheng, P. Zhang, W. Tian, J. Chen and Z. Sun, *J. Mater. Sci.*, 2019, **54**, 11991–11999.
83 M. T. P. Rigby-Bell, V. Natu, M. Sokol, D. J. Kelly, D. G. Hopkinson, Y. Zou, J. R. T. Bird, L. J. Evitts, M. Smith, C. P. Race, P. Frankel, S. J. Haigh and M. W. Barsoum, *RSC Adv.*, 2021, **11**, 3110–3114.
84 P. Urbankowski, B. Anasori, T. Makaryan, D. Er, S. Kota, P. L. Walsh, M. Zhao, V. B. Shenoy, M. W. Barsoum and Y. Gogotsi, *Nanoscale*, 2016, **8**, 11385–11391.
85 J. Zhu, M. Wang, M. Lyu, Y. Jiao, A. Du, B. Luo, I. Gentle and L. Wang, *ACS Appl. Nano Mater.*, 2018, **1**, 6854–6863.
86 A. Shahzad, K. Rasool, J. Iqbal, J. Jang, Y. Lim, B. Kim, J.-M. Oh and D. S. Lee, *Environ. Res.*, 2022, **205**, 112532.
87 S. Venkateshalu, J. Cherusseri, M. Karnan, K. S. Kumar, P. Kollu, M. Sathish, J. Thomas, S. K. Jeong and A. N. Grace, *ACS Omega*, 2020, **5**, 17983–17992.
88 B. Soundiraraju and B. K. George, *ACS Nano*, 2017, **11**, 8892–8900.
89 A. Djire, X. Wang, C. Xiao, O. C. Nwamba, M. V. Mirkin and N. R. Neale, *Adv. Funct. Mater.*, 2020, **30**, 2001136.
90 S. Zada, W. Dai, Z. Kai, H. Lu, X. Meng, Y. Zhang, Y. Cheng, F. Yan, P. Fu, X. Zhang and H. Dong, *Angew. Chem., Int. Ed.*, 2020, **59**, 6601–6606.
91 P. Urbankowski, B. Anasori, K. Hantanasirisakul, L. Yang, L. Zhang, B. Haines, S. J. May, S. J. L. Billinge and Y. Gogotsi, *Nanoscale*, 2017, **9**, 17722–17730.
92 H. Gao, J. Cao, T. Li, W. Luo, M. Gray, N. Kumar, K. S. Burch and X. Ling, *Chem. Mater.*, 2022, **34**, 351–357.
93 X.-H. Zha, J. Yin, Y. Zhou, Q. Huang, K. Luo, J. Lang, J. S. Francisco, J. He and S. Du, *J. Phys. Chem. C*, 2016, **120**, 15082–15088.
94 K. Kotmool, T. Kaewmaraya, T. Hussain, R. Ahuja, W. Luo and T. Bovornratanaraks, *Phys. Chem. Chem. Phys.*, 2022, **24**, 17862–17869.
95 K. Wang, H. Jin, H. Li, Z. Mao, L. Tang, D. Huang, J.-H. Liao and J. Zhang, *Surf. Interfaces*, 2022, **29**, 101711.
96 Q. Sun, Z. Fu and Z. Yang, *J. Magn. Magn. Mater.*, 2020, **514**, 167141.
97 X. Wang, S. Lin, H. Tong, Y. Huang, P. Tong, B. Zhao, J. Dai, C. Liang, H. Wang, X. Zhu, Y. Sun and S. Dou, *Electrochim. Acta*, 2019, **307**, 414–421.
98 J. Zhou, S. Lin, Y. Huang, P. Tong, B. Zhao, X. Zhu and Y. Sun, *Chem. Eng. J.*, 2019, **373**, 203–212.
99 C.-F. Du, X. Sun, H. Yu, W. Fang, Y. Jing, Y. Wang, S. Li, X. Liu and Q. Yan, *InfoMat*, 2020, **2**, 950–959.
100 K. Fan, Y. Ying, X. Luo and H. Huang, *J. Mater. Chem. A*, 2021, **9**, 25391–25398.
101 Z. Jing, H. Wang, X. Feng, B. Xiao, Y. Ding, K. Wu and Y. Cheng, *J. Phys. Chem. Lett.*, 2019, **10**, 5721–5728.
102 M. Han, C. E. Shuck, R. Rakhmanov, D. Parchment, B. Anasori, C. M. Koo, G. Friedman and Y. Gogotsi, *ACS Nano*, 2020, **14**, 5008–5016.
103 D. Pinto, B. Anasori, H. Avireddy, C. E. Shuck, K. Hantanasirisakul, G. Deysher, J. R. Morante, W. Porzio, H. N. Alshareef and Y. Gogotsi, *J. Mater. Chem. A*, 2020, **8**, 8957–8968.
104 H. Xu, R. Zheng, D. Du, L. Ren, R. Li, X. Wen, C. Zhao and C. Shu, *Appl. Mater. Today*, 2022, **27**, 101464.
105 S. Wang, Y. Wang, Q. Zhou, X. Li, Y. Li, Y. Liu, Y. Sun, T. Wang, L.-C. Xu and Y. Wang, *Phys. Chem. Chem. Phys.*, 2021, **23**, 3898–3904.
106 N. M. Caffrey, *Nanoscale*, 2018, **10**, 13520–13530.
107 Y. Wang, J. Shen, L.-C. Xu, Z. Yang, R. Li, R. Liu and X. Li, *Phys. Chem. Chem. Phys.*, 2019, **21**, 18559–18568.
108 T. Wang, Y. Liu, X. Zhang, J. Wang, Y. Zhang, Y. Li, Y. Zhu, G. Li and X. Wang, *ACS Appl. Mater. Interfaces*, 2021, **13**, 56085–56094.
109 Z. Chen, X. Yang, X. Qiao, N. Zhang, C. Zhang, Z. Ma and H. Wang, *J. Phys. Chem. Lett.*, 2020, **11**, 885–890.
110 M. Iqbal, J. Fatheema, Q. Noor, M. Rani, M. Mumtaz, R.-K. Zheng, S. A. Khan and S. Rizwan, *Mater. Today Chem.*, 2020, **16**, 100271.
111 H. Tan, C. Wang, H. Duan, J. Tian, Q. Ji, Y. Lu, F. Hu, W. Hu, G. Li, N. Li, Y. Wang, W. Chu, Z. Sun and W. Yan, *ACS Appl. Mater. Interfaces*, 2021, **13**, 33363–33370.
112 K. Luo, X.-H. Zha, Y. Zhou, Q. Huang, S. Zhou and S. Du, *Int. J. Quantum Chem.*, 2020, **120**, e26409.
113 Q. Gao and H. Zhang, *Nanoscale*, 2020, **12**, 5995–6001.
114 C. Si, J. Zhou and Z. Sun, *ACS Appl. Mater. Interfaces*, 2015, **7**, 17510–17515.
115 R. M. Ronchi, J. T. Arantes and S. F. Santos, *Ceram. Int.*, 2019, **45**, 18167–18188.
116 J. Lee, S.-Y. Kwon and J. H. Lee, *J. Mater. Chem. C*, 2021, **9**, 15346–15353.
117 Y. Wang, Y. Wang, K. Chen, K. Qi, T. Xue, H. Zhang, J. He and S. Xiao, *ACS Nano*, 2020, **14**, 10492–10502.
118 L. Gao, C. Ma, S. Wei, A. V. Kuklin, H. Zhang and H. Ågren, *ACS Nano*, 2021, **15**, 954–965.
119 M. Liu, J. Wu, C. Wang, Z. Sun, Z. Fan and C. Xin, *Solid State Commun.*, 2022, **341**, 114585.
120 S. Wang, C. Guan, Z. Zhao, R. Wang, Y. Tian and Y. Du, *Phys. Status Solidi B*, 2019, **256**, 1800457.
121 A. Lipatov, M. Alhabeb, H. Lu, S. Zhao, M. J. Loes, N. S. Vorobeva, Y. Dall'Agnese, Y. Gao, A. Gruverman, Y. Gogotsi and A. Sinitskii, *Adv. Electron. Mater.*, 2020, **6**, 1901382.
122 T. Hu, J. Yang, W. Li, X. Wang and C. M. Li, *Phys. Chem. Chem. Phys.*, 2020, **22**, 2115–2121.
123 M.-C. Liu, Y.-S. Zhang, B.-M. Zhang, D.-T. Zhang, C.-Y. Tian, L.-B. Kong and Y.-X. Hu, *Renewable Energy*, 2021, **169**, 573–581.
124 F. Liu, Y. Liu, X. Zhao, K. Liu, H. Yin and L.-Z. Fan, *Small*, 2020, **16**, 1906076.
125 X. Bin, M. Sheng, Y. Luo and W. Que, *Adv. Mater. Interfaces*, 2022, **9**, 2200231.

126 C.-F. Du, L. Yang, K. Tang, W. Fang, X. Zhao, Q. Liang, X. Liu, H. Yu, W. Qi and Q. Yan, *Mater. Chem. Front.*, 2021, **5**, 2338–2346.
127 W.-N. Zhao, N. Yun, Z.-H. Dai and Y.-F. Li, *RSC Adv.*, 2020, **10**, 1261–1270.
128 B. Zhou, H. Yin, C. Dong, L. Sun, W. Feng, Y. Pu, X. Han, X. Li, D. Du, H. Xu and Y. Chen, *Adv. Sci.*, 2021, **8**, 2101043.
129 Q. Meng, J. Ma, Y. Zhang, Z. Li, A. Hu, J.-J. Kai and J. Fan, *J. Mater. Chem. A*, 2018, **6**, 13652–13660.
130 X.-H. Zha, X. Ma, J.-T. Luo and C. Fu, *Nanoscale*, 2022, **14**, 10549–10558.
131 S. Zhao, X. Meng, K. Zhu, F. Du, G. Chen, Y. Wei, Y. Gogotsi and Y. Gao, *Energy Storage Mater.*, 2017, **8**, 42–48.
132 Z. Yang, Y. Zheng, W. Li and J. Zhang, *Nanoscale*, 2021, **13**, 11534–11543.
133 Z. Yang, Y. Zheng, W. Li and J. Zhang, *J. Comput. Chem.*, 2019, **40**, 1352–1359.
134 O. Mashtalir, M. R. Lukatskaya, M.-Q. Zhao, M. W. Barsoum and Y. Gogotsi, *Adv. Mater.*, 2015, **27**, 3501–3506.
135 D. Sun, M. Wang, Z. Li, G. Fan, L.-Z. Fan and A. Zhou, *Electrochem. Commun.*, 2014, **47**, 80–83.
136 M. Naguib, R. A. Adams, Y. Zhao, D. Zemlyanov, A. Varma, J. Nanda and V. G. Pol, *Chem. Commun.*, 2017, **53**, 6883–6886.
137 A. Rafieerad, A. Amiri, G. L. Sequiera, W. Yan, Y. Chen, A. A. Polycarpou and S. Dhingra, *Adv. Funct. Mater.*, 2021, **31**, 2100015.
138 R. Syamsai and A. N. Grace, *J. Alloys Compd.*, 2019, **792**, 1230–1238.
139 Y. Guan, R. Zhao, Y. Cong, K. Chen, J. Wu, H. Zhu, Z. Dong, Q. Zhang, G. Yuan, Y. Li, J. Zhang and X. Li, *Chem. Eng. J.*, 2022, **433**, 133582.
140 A. Djire, A. Bos, J. Liu, H. Zhang, E. M. Miller and N. R. Neale, *ACS Appl. Nano Mater.*, 2019, **2**, 2785–2795.
141 N. Chen, Y. Zhou, S. Zhang, H. Huang, C. Zhang, X. Zheng, X. Chu, H. Zhang, W. Yang and J. Chen, *Nano Energy*, 2021, **85**, 106007.
142 Z. W. Seh, K. D. Fredrickson, B. Anasori, J. Kibsgaard, A. L. Strickler, M. R. Lukatskaya, Y. Gogotsi, T. F. Jaramillo and A. Vojvodic, *ACS Energy Lett.*, 2016, **1**, 589–594.
143 S. Zhang, H. Zhuo, S. Li, Z. Bao, S. Deng, G. Zhuang, X. Zhong, Z. Wei, Z. Yao and J.-g. Wang, *Catal. Today*, 2021, **368**, 187–195.
144 Z. Wang, X. Zhang, Z. Ren, Y. Liu, J. Hu, H. Li, M. Gao, H. Pan and Y. Liu, *J. Mater. Chem. A*, 2019, **7**, 14244–14252.
145 S. Li, X. Que, X. Chen, T. Lin, L. Sheng, J. Peng, J. Li and M. Zhai, *ACS Appl. Energy Mater.*, 2020, **3**, 10882–10891.
146 K. Liang, A. Tabassum, M. Kothakonda, X. Zhang, R. Zhang, B. Kenney, B. D. Koplitz, J. Sun and M. Naguib, *Mater. Rep.: Energy*, 2022, **2**, 100075.
147 S. Jin, Z. Shi, H. Jing, L. Wang, Q. Hu, D. Chen, N. Li and A. Zhou, *ACS Appl. Energy Mater.*, 2021, **4**, 12754–12766.
148 Q. Wan, S. Li and J.-B. Liu, *ACS Appl. Mater. Interfaces*, 2018, **10**, 6369–6377.
149 Q. Shan, X. Mu, M. Alhabeb, C. E. Shuck, D. Pang, X. Zhao, X.-F. Chu, Y. Wei, F. Du, G. Chen, Y. Gogotsi, Y. Gao and Y. Dall'Agnese, *Electrochem. Commun.*, 2018, **96**, 103–107.
150 A. E. Ghazaly, W. Zheng, J. Halim, E. N. Tseng, P. O. Persson, B. Ahmed and J. Rosen, *Energy Storage Mater.*, 2021, **41**, 203–208.
151 J. Halim, S. Kota, M. R. Lukatskaya, M. Naguib, M.-Q. Zhao, E. J. Moon, J. Pitock, J. Nanda, S. J. May, Y. Gogotsi and M. W. Barsoum, *Adv. Funct. Mater.*, 2016, **26**, 3118–3127.
152 Y. Cheng, J. Dai, Y. Song and Y. Zhang, *ACS Appl. Energy Mater.*, 2019, **2**, 6851–6859.
153 Y. Xiao and W. Zhang, *Nanoscale*, 2020, **12**, 7660–7673.
154 Y. Cheng, L. Wang, Y. Li, Y. Song and Y. Zhang, *J. Phys. Chem. C*, 2019, **123**, 15629–15636.
155 W. Yang, Y. Cheng, M. Jiang, S. Jiang, R. Liu, J. Lu, L. Du, P. Li and C. Wang, *Sens. Actuators, B*, 2022, **369**, 132391.
156 Z. Guo, J. Zhou, L. Zhu and Z. Sun, *J. Mater. Chem. A*, 2016, **4**, 11446–11452.
157 M. Khazaei, A. Ranjbar, M. Arai and S. Yunoki, *Phys. Rev. B*, 2016, **94**, 125152.
158 L. Wang, L. Yuan, K. Chen, Y. Zhang, Q. Deng, S. Du, Q. Huang, L. Zheng, J. Zhang, Z. Chai, M. W. Barsoum, X. Wang and W. Shi, *ACS Appl. Mater. Interfaces*, 2016, **8**, 16396–16403.
159 M. Han, C. E. Shuck, A. Singh, Y. Yang, A. C. Foucher, A. Goad, B. McBride, S. J. May, V. B. Shenoy, E. A. Stach and Y. Gogotsi, *Cell Rep. Phys. Sci.*, 2022, **3**, 101073.
160 X.-H. Li, X.-Y. Su, R.-Z. Zhang, C.-H. Xing and Z.-L. Zhu, *J. Phys. Chem. Solids*, 2020, **137**, 109218.
161 H. Zhang, G. Yang, X. Zuo, H. Tang, Q. Yang and G. Li, *J. Mater. Chem. A*, 2016, **4**, 12913–12920.
162 S. Li, A. Cui, B. Sun, G. Liu and B. Xu, *Solid State Commun.*, 2021, **336**, 114411.
163 G. Wang and Y. Liao, *Appl. Surf. Sci.*, 2017, **426**, 804–811.
164 Y. Yue, B. Wang, N. Miao, C. Jiang, H. Lu, B. Zhang, Y. Wu, J. Ren and M. Wang, *Ceram. Int.*, 2021, **47**, 2367–2373.
165 C. Zhan, W. Sun, P. R. C. Kent, M. Naguib, Y. Gogotsi and D.-e. Jiang, *J. Phys. Chem. C*, 2019, **123**, 315–321.
166 Q. Sun, J. Li, Y. Li, Z. Yang and R. Wu, *Appl. Phys. Lett.*, 2021, **119**, 062404.
167 H. Kumar, N. C. Frey, L. Dong, B. Anasori, Y. Gogotsi and V. B. Shenoy, *ACS Nano*, 2017, **11**, 7648–7655.
168 N. C. Frey, J. Wang, G. I. Vega Bellido, B. Anasori, Y. Gogotsi and V. B. Shenoy, *ACS Nano*, 2019, **13**, 3031–3041.
169 M. Khazaei, A. Ranjbar, K. Esfarjani, D. Bogdanovski, R. Dronskowski and S. Yunoki, *Phys. Chem. Chem. Phys.*, 2018, **20**, 8579–8592.
170 Z. Wang, N. Ding, C. Gui, S.-S. Wang, M. An and S. Dong, *Phys. Rev. Mater.*, 2021, **5**, 074408.
171 C. Ougherb, T. Ouahrani, M. Badawi and Á. Morales-García, *Phys. Chem. Chem. Phys.*, 2022, **24**, 7243–7252.
172 Y. Zhang, B. Sa, N. Miao, J. Zhou and Z. Sun, *J. Mater. Chem. A*, 2021, **9**, 10882–10892.
173 S. Zhao, W. Kang and J. Xue, *Appl. Phys. Lett.*, 2014, **104**, 133106.
174 Y. Lee, S. B. Cho and Y.-C. Chung, *ACS Appl. Mater. Interfaces*, 2014, **6**, 14724–14728.

175 H. Weng, A. Ranjbar, Y. Liang, Z. Song, M. Khazaei, S. Yunoki, M. Arai, Y. Kawazoe, Z. Fang and X. Dai, *Phys. Rev. B: Condens. Matter Mater. Phys.*, 2015, **92**, 075436.
176 J. Wang, L. Bai, C. Yao and L. Niu, *Phys. Lett. A*, 2022, **424**, 127842.
177 L. R. Johnson, S. Sridhar, L. Zhang, K. D. Fredrickson, A. S. Raman, J. Jang, C. Leach, A. Padmanabhan, C. C. Price, N. C. Frey, A. Raizada, V. Rajaraman, S. A. Saiprasad, X. Tang and A. Vojvodic, *ACS Catal.*, 2020, **10**, 253–264.
178 X. Lv, W. Wei, Q. Sun, L. Yu, B. Huang and Y. Dai, *ChemPhysChem*, 2017, **18**, 1627–1634.
179 B. Wei, Z. Fu, D. Legut, T. C. Germann, Q. Zhang, S. Du, H. Zhang, J. S. Francisco and R. Zhang, *J. Phys. Chem. C*, 2021, **125**, 4477–4488.
180 L. Dong, H. Kumar, B. Anasori, Y. Gogotsi and V. B. Shenoy, *J. Phys. Chem. Lett.*, 2017, **8**, 422–428.
181 H. Liu, H. Wang, Z. Jing, K. Wu, Y. Cheng and B. Xiao, *J. Phys. Chem. C*, 2020, **124**, 25769–25774.
182 M. Dahlqvist and J. Rosen, *Phys. Chem. Chem. Phys.*, 2015, **17**, 31810–31821.
183 M. Dahlqvist and J. Rosen, *Nanoscale*, 2020, **12**, 785–794.
184 T. L. Tan, H. M. Jin, M. B. Sullivan, B. Anasori and Y. Gogotsi, *ACS Nano*, 2017, **11**, 4407–4418.
185 D. Jin, L. R. Johnson, A. S. Raman, X. Ming, Y. Gao, F. Du, Y. Wei, G. Chen, A. Vojvodic, Y. Gogotsi and X. Meng, *J. Phys. Chem. C*, 2020, **124**, 10584–10592.
186 J. Yang, X. Luo, X. Zhou, S. Zhang, J. Liu, Y. Xie, L. Lv and L. Chen, *Comput. Mater. Sci.*, 2017, **139**, 313–319.
187 Y. Zhang, Z. Cui, B. Sa, N. Miao, J. Zhou and Z. Sun, *Nanoscale Horiz.*, 2022, **7**, 276–287.
188 W. Sun, Y. Xie and P. R. C. Kent, *Nanoscale*, 2018, **10**, 11962–11968.
189 Z. Zeng, X. Chen, K. Weng, Y. Wu, P. Zhang, J. Jiang and N. Li, *npj Comput. Mater.*, 2021, **7**, 80.
190 Q. Tao, J. Lu, M. Dahlqvist, A. Mockute, S. Calder, A. Petruhins, R. Meshkian, O. Rivin, D. Potashnikov, E. a. N. Caspi, H. Shaked, A. Hoser, C. Opagiste, R.-M. Galera, R. Salikhov, U. Wiedwald, C. Ritter, A. R. Wildes, B. Johansson, L. Hultman, M. Farle, M. W. Barsoum and J. Rosen, *Chem. Mater.*, 2019, **31**, 2476–2485.
191 M. Dahlqvist, J. Lu, R. Meshkian, Q. Tao, L. Hultman and J. Rosen, *Sci. Adv.*, 2017, **3**, e1700642.
192 K. J. Griffith, M. A. Hope, P. J. Reeves, M. Anayee, Y. Gogotsi and C. P. Grey, *J. Am. Chem. Soc.*, 2020, **142**, 18924–18935.
193 C. E. Shuck, A. Sarycheva, M. Anayee, A. Levitt, Y. Zhu, S. Uzun, V. Balitskiy, V. Zahorodna, O. Gogotsi and Y. Gogotsi, *Adv. Eng. Mater.*, 2020, **22**, 1901241.
194 A. Iqbal, J. Hong, T. Y. Ko and C. M. Koo, *Nano Convergence*, 2021, **8**, 9.

